Journal of Materials Chemistry A

ROYAL SOCIETY OF CHEMISTRY

REVIEW

View Article Online
View Journal | View Issue

Cite this: J. Mater. Chem. A, 2023, 11, 11048

The journey of iron-based electrocatalytic materials for nitrogen reduction reaction: from current status to future prospects

Yi-Han Wang,[b] Ji-Hong Dong,[a] Zhenquan Tan,[a] Xiao-Feng Wang[c] and Xue-Zhi Song *[a]

Ammonia (NH_3) is the most important chemical and carbon-free energy carrier, which is currently mainly produced by the energy-intensive Haber–Bosch process at high temperatures and pressures. In the spirit of global carbon neutrality and sustainable development, electrochemical nitrogen reduction reaction (NRR) is expected as a promising alternative to the traditional Haber–Bosch process for industrial ammonia production due to both low energy consumption and zero emission of carbon dioxide. However, further breakthroughs in electrochemical NRR strongly depend on the efficiency and selectivity of electrocatalysts. The element Fe has been found to be an important component in nitrogenase enzymes, generating extensive research interest. As one of the most cost-effective and abundant transition metals, iron-based materials have presented great potential for electrochemical NRR. In this review, we summarize recent advances in iron-based materials (including its oxides, chalcogenides, borides, single Fe-atom catalysts, and bimetallic catalysts especially for Fe–Mo-based compounds) towards highly efficient N_2-to-NH_3 conversion under ambient conditions. Based on recent theoretical and experimental studies, we focus on the structure–property relationship. Strategies to boost NRR performances and perspectives for future developments are comprehensively presented in synthetic protocols, structure modification, activity/selectivity enhancement, and reaction mechanisms to provide insightful guidance for the field of NRR studies.

Received 14th March 2023
Accepted 26th April 2023

DOI: 10.1039/d3ta01548c

rsc.li/materials-a

1. Introduction

Ammonia is one of the most principal chemicals and carbon-free energy carriers and also plays an indispensable role in sustaining life.[1] Its worldwide annual production is estimated to be 150–200 million tons, providing a hint of insufficiency due to the booming human demands.[2] Despite the fact that N_2 makes up more than 78% of the atmosphere, it cannot be

[a]State Key Laboratory of Fine Chemicals, School of Chemical Engineering, Dalian University of Technology, Dalian 116024, China. E-mail: songxz@dlut.edu.cn

[b]Leicester International Institute, Dalian University of Technology, Panjin 124221, China

[c]Key Laboratory of Materials Modification by Laser, Ion and Electron Beams, Ministry of Education, School of Physics, Dalian University of Technology, Dalian 116024, China

Yi-Han Wang is pursuing his B.S. degree at Dalian University of Technology. His research focuses on the design and preparation of electrocatalysts for NRR under the supervision of Dr Xue-Zhi Song.

Ji-Hong Dong received her B.S. degree in chemical engineering from Dalian University of Technology. Now, she is pursuing the M.S. degree under the supervision of Associate Prof. Xue-Zhi Song. Her research focuses on the design and preparation of electrocatalysts for NRR.

directly utilized by industry or living organisms.[3] Modern industrial large-scale ammonia production still relies on the Haber–Bosch process, which was invented in the 20th century and has contributed to human society for hundreds of years.[4] However, the Haber–Bosch technology entails thermocatalytic conversion of N_2 and H_2 at high temperature (400–500 °C) and intense pressure (200–300 atm).[5–7] These conditions determine that Haber–Bosch process is extremely energy-intensive, accounting for 2% of the global energy consumption, accompanied by large greenhouse gas emissions (300–400 million tons of CO_2 annually).[8,9] Therefore, a greener and more efficient NH_3 synthesis method under mild conditions is desired to support the world's sustainable development and carbon neutrality goals.[10,11]

Currently, it has been proven that biocatalysis, photocatalysis, and electrocatalysis are clean pathways for ammonia synthesis from nitrogen reduction.[12–15] Electrochemical synthesis of ammonia is considered the most promising alternative to the Haber–Bosch process, due to its mild and stable reaction conditions, abundant hydrogen source (direct extraction from electrolyte instead of fossil fuels), zero CO_2 emissions, and flexible and easily-controlled production process by adjusting external parameters.[16] In the electrochemical ammonia synthesis, NH_3 is produced from N_2 and H_2O under ambient conditions by inputting electrical energy, with the catalyst playing a decisive role. In fact, the breakthrough development of the electrochemical ammonia synthesis is hampered by some inherent limitations: (1) the ultra-low solubility of N_2 in water (6.8×10^{-4} M, 1.01×10^5 Pa, 298 K) is not conducive to maintaining high reactant concentrations, resulting in the unsatisfying ammonia production rate. (2) Low Faraday efficiency (FE). The improvement of FE is hindered by competing hydrogen evolution reactions (HER).[17] The electrochemical NRR and HER are both thermodynamically available under reaction conditions. Not only that but HER is preferred from a kinetic point of view because it is a feasible two-electron process. By comparison, electrocatalytic NRR is a multi-step kinetic retardation process, involving six protons and six electrons as well as the activation of inert nitrogen bonds.[18] (3) The stability and ammonia yield rate of the catalyst is challenging to fulfill the requirements of industrial production.[19]

From the molecular mechanistic level, the primary challenge of NRR results from the inertness of the N≡N triple bond, which is the strongest among the diatomic molecules and lacks a permanent dipole.[20] A high energy input of 945 kJ mol^{-1} is required to cleave the N≡N triple bond, which well explains the harsh conditions of the Haber–Bosch process.[21] The kinetically difficult electron transfer reaction and the thermodynamically forbidden protonation of N_2 to N_2H^+ also make the electrochemical NRR more difficult.[22] Researchers have developed numerous catalysts with good performances to address the above challenges of electrochemical NRR, including noble metals, transition metal (TM) compounds, and metal-free materials.[23–33] Among these materials, iron-based catalysts stand out as a non-noble metal protagonist with the advantages of low cost, large-scale industrial synthesis, and high catalytic efficiency. Iron (Fe) is the only element that coexists among the three biological nitrogen-fixing enzymes, suggesting that iron plays an important role in NRR.[21] Moreover, Fe is an active metal easy to be compounded with other elements, such as modifying it into nitrides, hydroxides, oxides, sulfides, and phosphides, which may exhibit distinguished catalytic activation and stability. More importantly, the electronic configuration of Fe provides good solutions to activate the N_2 molecule. As a transition metal, the Fe atom has an electronic configuration of $3d^6 4s^2$, indicating four unpaired d-spin electrons. These

Zhenquan Tan is a Full Professor at School of Chemical Engineering in Dalian University of Technology (China). He received his B.S. degree in chemistry at Peking University (China) in 2002, and received his PhD degree in chemistry from Tohoku University (Japan) in 2008. His current research interests are focused on the inorganic nanomaterials and their applications in photo-/electrocatalysis, energy storage and conversion, and anti-tumor nanodrug delivery systems.

Xiao-Feng Wang is an associate professor in Dalian University of Technology, China. She received her PhD degree in Material Physics and Chemistry from Shandong University, China in 2014. She was a visiting scholar at A. J. Drexel Nanomaterials Institute, Drexel University, during 2018. Her research interests focus on nanomaterials and their applications in gas sensors and catalysis.

Xue-Zhi Song received his B.S. degree from Lanzhou University (China) in 2009. He completed his PhD degree in Changchun Institute of Applied Chemistry, Chinese Academy of Sciences (China) in 2015. He is currently an Associate Professor in Dalian University of Technology (China). His research interest focuses on functional inorganic nanomaterials for electrocatalysis in HER, OER, and NRR.

abundant d-orbital electrons and unoccupied orbitals activate the inert N≡N triple bond by driving the well-known donation-acceptance process.[34–40] To be more precise, the empty or half-occupied orbitals in Fe allow σ donation to accommodate electrons from N_2 bonding orbitals (σ orbitals). Meanwhile, the affluent d-electrons in Fe atoms could be injected into the antibonding orbitals (π* orbitals) in N_2 by back-donation. As a result, the loss of electrons from the bonding orbitals and the injection of electrons into antibonding orbitals greatly destabilize N_2 and expedite the break of the N≡N bond. It is acknowledged that the NRR activity of the transition metals is usually closely related to the occupancy of e_g and t_{2g} orbitals in the catalyst. Fe atom has a manipulable local spin state of t2g4eg2. Both experimental and theoretical analysis indicate that the heightened e_g electrons penetration to the antibonding π-orbital of N_2 and regulation of the adsorption strength of nitrogen species can be realized by customized spin-polarization configuration.[41] Moreover, the electron jump between high-spin iron and ferrous in the appropriate Fe lattice provides good electronic conductivity and poor adsorption of protons, which may lead to more ideal efficiency and selectivity towards NRR.[42,43] From a macroscopic view in the design of catalysts, Fe is easily modified for various construction strategies, including vacancy engineering, heteroatom doping, facet control, single atom dispersion, and even metal–organic frameworks (MOFs).[21,44–46] These strategies usually enhance N_2 adsorption by redistribution of charge density in the catalyst and provide more active sites to improve catalytic efficiency of NRR.[47,48]

Based on these facts, this review introduces the recent progress of iron-based catalysts for electrocatalytic NRR under ambient conditions. Firstly, we systematically present the recent advances on iron catalysts for NRR according to the types of iron compounds, which are iron oxides, iron sulfides, Fe-containing bimetallic materials, especially iron-molybdenum compounds, iron borides, and single iron atoms catalysts (Fig. 1). Furthermore, we analyze the available approaches to design advanced electronic and interface structures for different types of iron-based catalysts and relationships between structures and properties from experimental and theoretical perspectives. Finally, we prospect the challenges and potential strategies for further enhancement of NRR performance in terms of FE, ammonia yield, and selectivity.

2. Fundamental principles of the electrocatalytic NRR

Understanding the characteristics of nitrogen molecules and the reaction mechanism of NRR is the basis of superior NRR electrocatalyst design.

2.1 Properties of N_2

The very stable nitrogen molecule is formed by the linear combination of two N atoms, each of them has five valence electrons, arranged in the configuration of $2s^2 2p^3$. According to molecular orbital theory, the valent orbitals of N_2 molecules are composed of four bonding orbitals (σ_{2s}, σ_{2p}, and two π) and four antibonding orbitals (σ^*_{2s}, σ^*_{2p}, and two π*), in which two π* orbitals and one σ^*_{2p} orbital display an empty state, while other orbitals are fully occupied by the coupled spin electrons (Fig. 2A).[61] The three occupied σ_{2p} and two π orbital bonds also contribute to the high-energy triple bond.[62] The large energy gap (10.82 eV) between the lowest unoccupied molecular orbital (LUMO) and the highest occupied molecular orbital (HOMO) of N_2, the high ionization potential (15.58 eV), and the negative electron affinity (−1.9 eV) all account for the resistance of N_2 to Lewis acid/base and electron-transfer processes.[63–68] In the view of thermodynamics, NRR is practicable with the overall negative Gibbs free energy. In fact, as the first step of the overall reaction, the adsorption and activation of N_2 are intractable since their non-polarity and high stability. The initial endothermic protonation of N_2 to form N_2H^+ (ΔH^0 = +37.6 kJ mol^{-1}) is thermodynamically forbidden. Another challenge is the kinetically complex nitrogen hydrogenation process, which involves multiple electron transfers and complex intermediates.[44] These intrinsic features render the N_2 fixation *via* electro-reduction of N_2 to NH_3 of great challenge and difficulty. Nevertheless, the N≡N bond can be weakened by σ donation and π back-donation between N_2 and Fe atoms (Fig. 2B).

This will provide guidance for the rational design of catalytic active sites starting from addressing the intrinsic inertness of N_2.

2.2 NRR mechanisms

The net NRR can be expressed as the equations below:

In acidic media

$$N_2 + 6H^+ + 6e^- \rightarrow 2NH_3$$

In basic media

$$N_2 + 6H_2O + 6e^- \rightarrow 2NH_3 + 6OH^-$$

The detailed NRR process mainly involves the following three steps: (i) the chemisorption of N_2 molecules on the active sites; (ii) the dissociation and hydrogenation of nitrogen; and (iii) the desorption of the ammonia molecules from the catalyst surface. According to the adsorption configurations and the hydrogenation reaction sequences of nitrogen, two basic pathways have been proposed (i) the dissociative mechanism and (ii) the associative mechanism (Fig. 2C).[69–73]

2.2.1 Dissociative mechanism. In the typical dissociative pathway, the nitrogen molecule is cleaved into two independent nitrogen atoms and adsorbed on the catalyst surface for subsequent hydrogenation. *NH_3 is derived from *N *via* *NH and *NH_2, after three successive hydrogenation steps. However, the direct breaking of the N≡N bond has a large energy barrier and usually occurs only at high temperatures (such as in the Haber–Bosch process), which is unlikely to be a favorable pathway for electrochemical NRR under ambient conditions.

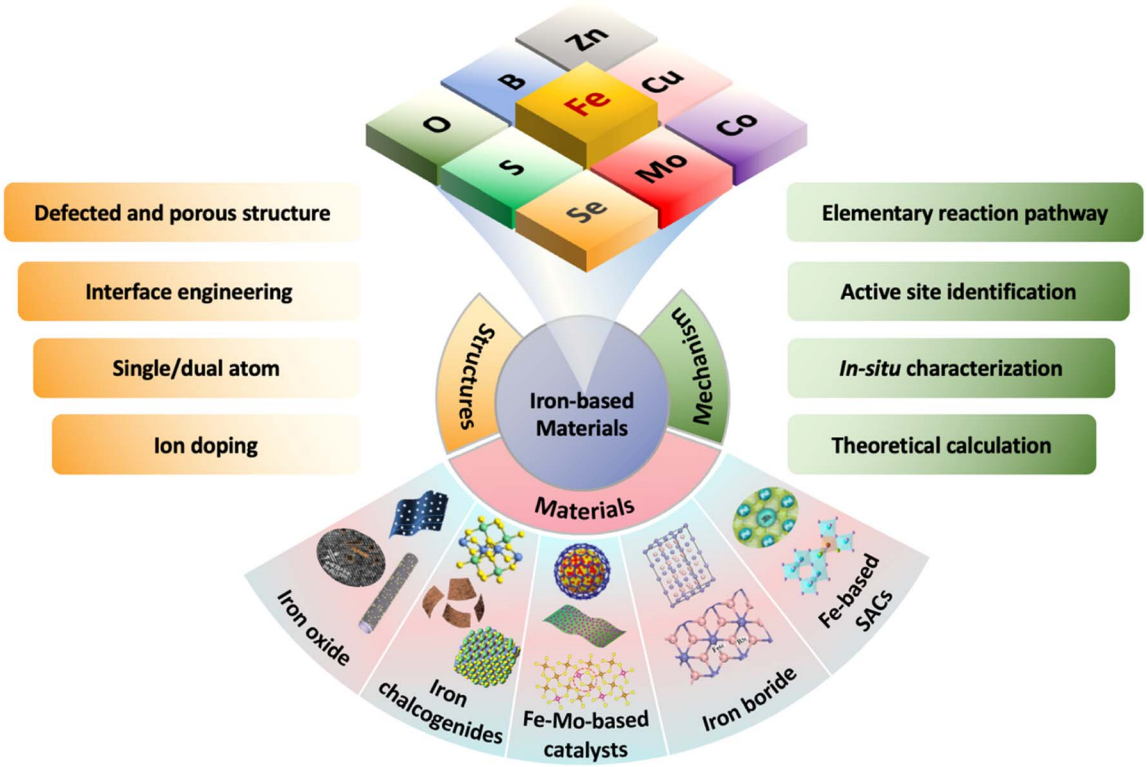

Fig. 1 Scheme organization of the main contents of this review. Iron oxides: reproduced with permission: copyright 2021, Elsevier.[49] Copyright 2022, Wiley-VCH.[50] Copyright 2022, Royal Society of Chemistry.[51] Iron chalcogenides: reproduced with permission: copyright 2021, Elsevier.[52] Copyright 2021, Wiley-VCH.[53] Fe–Mo-based catalysts: reproduced with permission: copyright 2019, Elsevier.[54] Copyright 2020, Royal Society of Chemistry.[55] Copyright 2020, American Chemical Society.[56] Iron borides: reproduced with permission: copyright 2020, Elsevier.[57] Copyright 2019, Royal Society of Chemistry.[58] Fe-based SACs : reproduced with permission: copyright 2022, Wiley-VCH.[59,60]

2.2.2 Associative mechanism. In contrast, the gradual cleavage of the N≡N bond provides thermodynamically favorable pathways, namely, associative pathways, where the hydrogenation of N_2 occurs prior to the breaking of the N≡N bond. The two different adsorption modes (end-on and side-on) initiate varying associative pathways. It can be classified into three possible reaction pathways depending on the binding pattern of N_2 and the hydrogenation sequence. As for the end-on adsorbed N_2, it accepts an electron and proton to generate $*N_2H$, and then both the alternative pathway and the distal pathway can proceed.

Associative-alternative pathway. In the alternative pathway, both N atoms are reduced successively with alternative hydrogenation. The N≡N bond remains unbroken until the last hydrogenation and two NH_3 molecules are almost concurrently desorbed.

Associative-distal pathway. In the distal pathway, the distal N atom accomplishes hydrogenation to form and release an NH_3 molecule before any hydrogenation of the proximal N atom.

Associative-enzymatic pathway. In this particular case, N_2 is absorbed in a side-on adsorption mode and each nitrogen atom is hydrogenated enzymatically, which is similar to the alternating pathway. Notably, this pathway is favored in the presence of biological nitrogenases and some catalysts that have a strong bind with N_2. The hydrazine (N_2H_4), formed as an intermediate of the enzymatic pathway, is mostly a minor product thanks to the high energy barrier of its desorption from the catalyst surface.[12] The enzymatic routes that occur on iron-based catalyst surfaces were reported in several works.[74–76]

In addition to the classical NRR pathways mentioned above, novel pathways have been discovered in practice by *in situ* spectroscopies.[77,78] Shao's group proposed a new two-step reaction pathway for NRR, based on surface-enhanced infrared-absorption spectroscopy and differential electrochemical mass spectrometry data.[78] In such a pathway, the absorbed nitrogen molecule reduces to $N_2H_2^*$ by a two-electron transfer process, followed by its desorption and decomposition to form NH_3 ($3N_2H_2 \rightarrow 2NH_3 + 2N_2$). These characterization techniques and findings provide important tools and new insights into the reaction mechanism of NRR on metal surfaces, which can inspire further understanding of the NRR mechanism and rational design of the more advanced electrocatalysts.

3. Iron-based electrocatalytic materials

Electrocatalysis is a surface-sensitive process, and surface and subsurface configurations directly affect catalytic performance.[80,81] Various material modification strategies, such as vacancies, defects, high-index facets (HIFs), and strains have

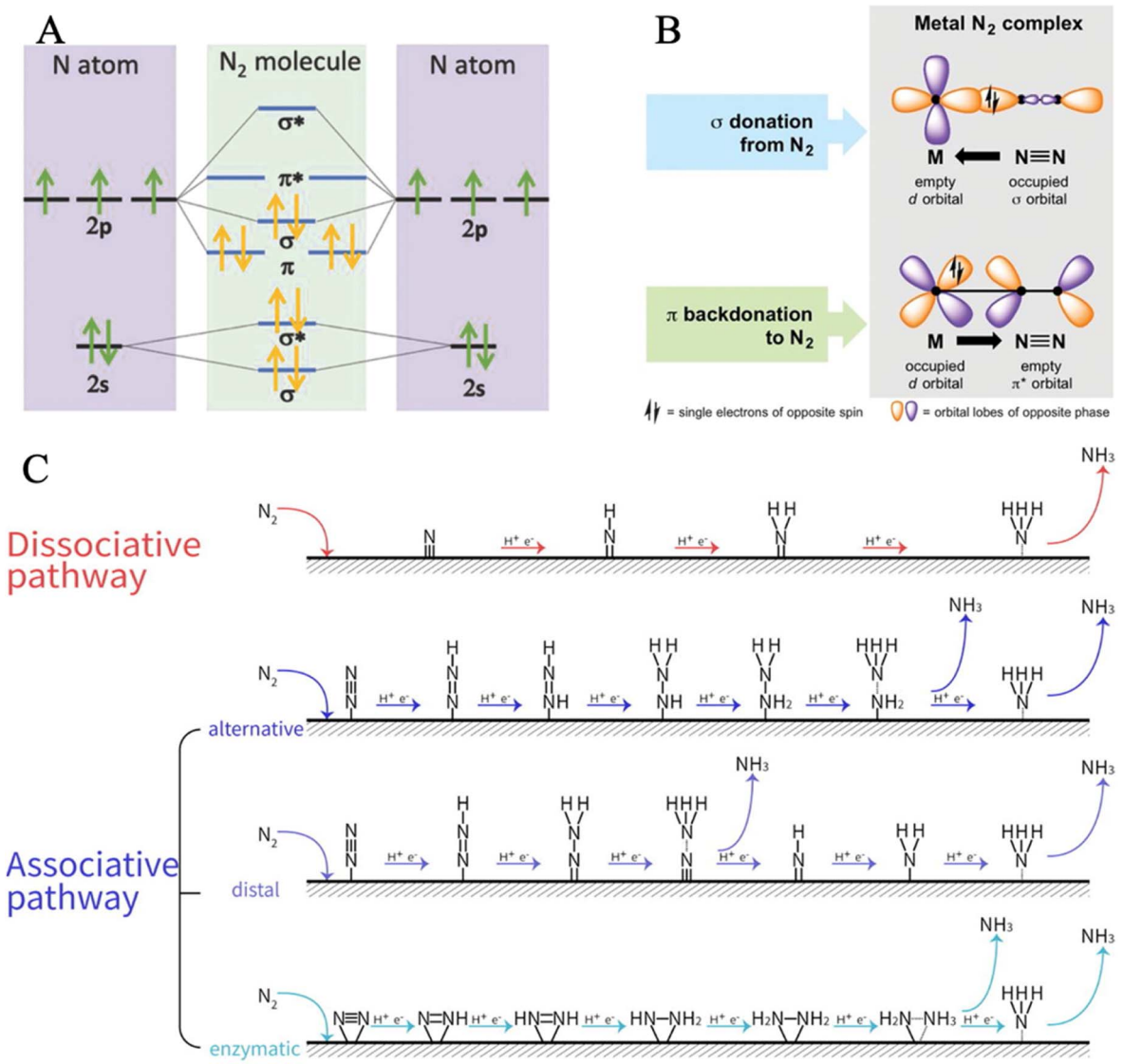

Fig. 2 (A) Diagram of N atomic orbitals and N_2 molecular orbital diagram. Reproduced with permission: copyright 2018, Wiley-VCH.[66] (B) Binding modes of N_2 molecules with transition metals. Reproduced with permission: copyright 2018, American Association for the Advancement of Science.[79] (C) Reaction pathways for the electrochemical nitrogen reduction to ammonia. Reproduced with permission: copyright 2021, Elsevier.[12]

been developed to design NRR catalysts, including iron-based catalysts.[44,82–86] These strategies will be introduced, respectively in the category/section to which they belong. Amongst them, defect and vacancy engineering (*e.g.*, oxygen vacancies (OVs), sulfur vacancies (SVs), and tellurium vacancies (TeVs)) are more common and effective to generate active sites and enhance intrinsic NRR activity for the following reasons. Firstly, by creating defects and vacancies in the catalyst, the electronic structure of the electrocatalyst can be manipulated to improve conductivity and promote N_2 adsorption and activation, thereby reducing the activation energy barrier.[87,88] Besides, the coordination environment of the metal centers can be adjusted to produce low-coordinated and unsaturated metal sites, thus increasing the extrinsic catalytic activity of the electrocatalyst by increasing the number of active sites.[89]

3.1 Iron oxide

Metal oxides are widely used in the field of chemical catalysis studies, due to their low cost, wide source, tunable activity, and environment benignity.[90] Interestingly, plenty of works about iron oxides and their derivatives for electrochemical ammonia synthesis have been reported, providing a wealth of experience for the further development and application of iron oxides as efficient NRR catalysts.[91–93] Iron oxides are suggested to offer good long-term durability and cycling stability in a neutral electrochemical environment.[49] Also, some works have pointed to the beneficial effects of pairing iron oxides with highly conductive catalyst substrates to accelerate electron transfer efficiency and achieve good electrochemical performance.[94,95] Iron oxides have the natural defect of OVs, tailoring their electronic structures and charge distribution for increasing the

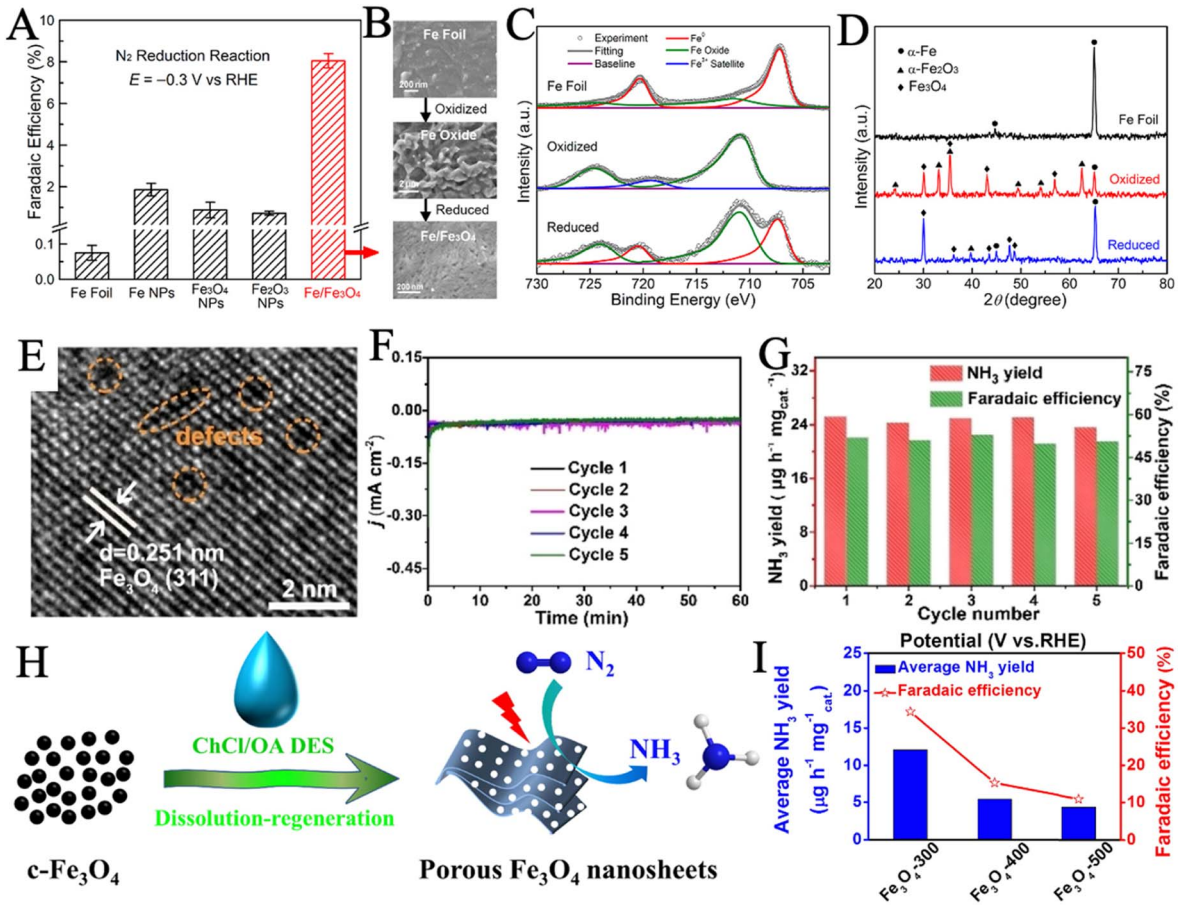

Fig. 3 (A) FE of Fe/Fe_3O_4 and several commercial iron materials. (B) SEM images of the Fe foil, the 300 °C oxidized sample, and the sample after the reduction. XPS spectra of the Fe 2p peaks (C) and grazing-incidence XRD patterns (D) of the three samples. Reproduced with permission: copyright 2018, American Chemical Society.[100] (E) HRTEM images of Fe–Fe_3O_4 catalyst. Chronoamperometry curves (F), NH_3 production rate and FE (G) of Fe–Fe_3O_4 catalyst during the 5 cycles tests. Reproduced with permission: copyright 2022, Wiley-VCH.[50] (H) Synthetic route schematic of porous Fe_3O_4 nanosheets. (I) Average NH_3 production rate and FEs (at −0.1 V) of samples were annealed at different temperatures. Reproduced with permission: copyright 2021, Elsevier.[49]

quantity of active sites with a modulated energy barrier. On the one hand, surface OVs could accommodate the electron-accumulating Lewis base as well as catalytically reactive unsaturated sites to guide NRR to proceed through pathways with low energy barriers. On the other hand, theoretical studies revealed that the electrons tend to accumulate around the valence band maximum of metal oxides with OVs, and thus facilitate N_2 adsorption and N_2 activation by stretching the N≡N triple bond.[96–99]

Stoichiometric Fe_3O_4 and Fe_2O_3 and their derived structures have been extensively studied as iron oxides for NRR electrocatalysis. Hu and coworkers reported a Fe/Fe_3O_4 hybrid catalyst *via* thermal oxidization of Fe foil and subsequent *in situ* electrochemical reduction (Fig. 3B).[100] X-ray photoelectron spectroscopy (XPS) (Fig. 3C) revealed the composition and chemical state changes of the surface layer in the three samples. The Fe^0 on the Fe foil surface was completely oxidized and then reduced to both Fe^0 and oxidic Fe components by the subsequent electrochemical reduction. Furthermore, the presence of α-Fe and Fe_3O_4 crystallites in the as-prepared catalyst was confirmed by X-ray diffraction (XRD) (Fig. 3D). Such Fe/Fe_3O_4 catalyst demonstrated significantly better NRR selectivity than several commercial iron materials (Fig. 3A), reaching an NH_3 yield of 0.19 μg cm^{-2} h^{-1} and a FE of 8.29% in the phosphate buffer solution. Similarly, Xie *et al.* developed a one-step green synthesis of Fe–Fe_3O_4 catalyst *via* the reduction of $FeSO_4$ in an aqueous solution using KBH_4.[50] High-resolution transmission electron microscope (HRTEM) image (Fig. 3E) depicted the presence of atom-vacancy defects in Fe–Fe_3O_4 nanocrystals, which resulted in the excellent NRR performance by enhancing the nitrogen adhesive ability. Electrochemical impedance spectroscopy (EIS) suggested that Fe–Fe_3O_4 had a significantly enhanced charge transfer capacity. During five cycle tests, no obvious changes in the current density curves (Fig. 3F), NH_3 yield rate, and FE (Fig. 3G) were observed, indicating the excellent stability of Fe–Fe_3O_4 for NRR. Porous structures with high specific surface area have been built to enhance the catalytic performance by increasing active surface area. In a recent study, Ying *et al.* reported porous Fe_3O_4 nanosheets *via* regeneration from deep eutectic solvent (DES) and subsequent

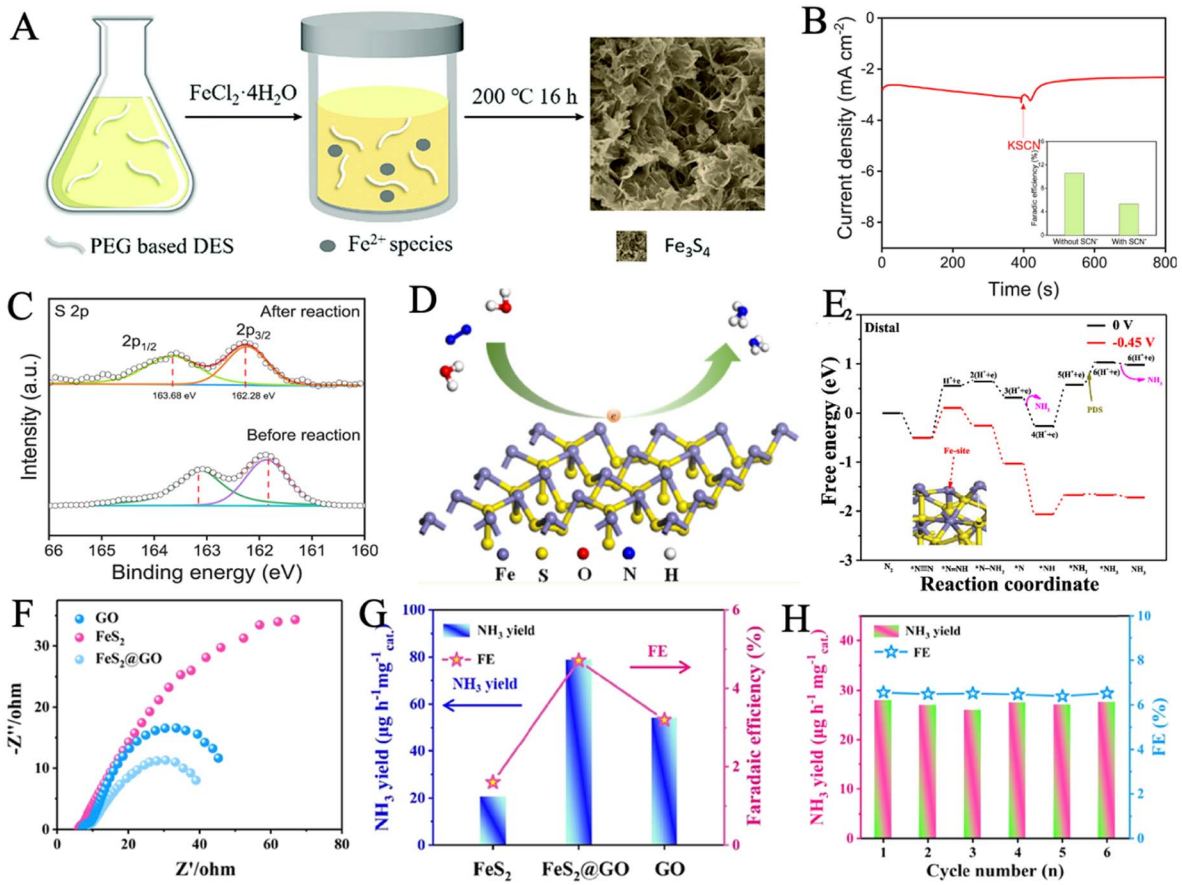

Fig. 4 (A) Schematic of the formation of Fe_3S_4 in the PEG based DES. Reproduced with permission: copyright 2018, Royal Society of Chemistry[123] (B) chronoamperometry curve of Vs-$FePS_3$ in N_2-saturated electrolyte with the addition of SCN^- ion. Inset: FEs with and without the SCN^- ion. (C) XPS spectra of S 2p of Vs-$FePS_3$ before and after NRR. Reproduced with permission: copyright 2021, Elsevier.[52] (D) Schematic diagram of coordination configuration in FeS_2. (E) Free energy profile for NRR in Fe atoms as the active sites. Reproduced with permission: copyright 2020, American Chemical Society.[126] (F) Nyquist plots and (G) ammonia yield and FE of FeS_2@GO, GO and FeS_2 at −0.3 V in N_2-saturated 0.1 M HCl solution. (H) Six-time recycling test of FeS_2@GO. Reproduced with permission: copyright 2021, American Chemical Society.[128]

annealing (Fig. 3H).[49] A series of annealing temperatures was applied, sample Fe_3O_4-300, which was sintered at 300 °C had the largest specific surface area (88.30 $m^2\ g^{-1}$), exhibiting an NH_3 yield rate of 12.09 μg h^{-1} mg_{cat}^{-1} and a remarkable FE of 34.38% (Fig. 3I).

Except for the widely studied aqueous electrolyte systems, advances of iron-based catalysts have also been made in non-aqueous electrolyte systems to address some inherent difficulties.[18,101,102] Ammonia electro-synthesis in aqueous systems suffer from low N_2 solubility and competitive HER.[103] Typically, the reduction of water to hydrogen occurs in the same region of potential with NRR, resulting in low FEs.[104] Calculations and experiments showed that nitrogen is much more soluble in some ionic liquids (ILs) than in water.[105,106] The improved N_2 solubility in IL electrolytes is an effective way to increase N_2 adsorption at the active sites.[11] Besides, ILs are hydrophobic and can serve as excellent non-aqueous substances because they can lower the water content at an optimal level to effectively restrain the evolution of H_2.[104] MacFarlane and coworkers practically explored the NRR performance of Fe deposited working electrode substrates (including fluorine-doped tin oxide glass, nickel foam, and stainless steel cloth) in a hydrophobic, high N_2-solubility IL electrolyte ([C_4mpyr][eFAP] and [$P_{6,6,6,14}$][eFAP], respectively).[104] The strong interaction between N_2 and $[eFAP]^-$ was proposed by DFT calculations, which explained the high solubility of N_2. This work also suggests the influence of the viscosity of ILs on electrochemical performance, that lower viscosity can support higher mass transport to produce higher current densities and yields. Although this NRR system achieved an incredibly high FE of 60%, the reduction currents obtained on low surface area substrates are too small and the yield needs to be improved for practical applications. In another work, MacFarlane's group further focused on the rational electrode–electrolyte design and demonstrated the effectiveness of using highly fluorinated solvents to realize efficient electrochemical ammonia synthesis.[107] The mixture of 1*H*,1*H*,5*H*-octafluoropentyl-1,1,2,2-tetrafluoroethyl ether and [C_4mpyr][eFAP] were chosen and characterized to determine the optimum solvent–IL ratio to achieve a maximum conductivity of 1.95 mS cm^{-1} and electrochemical window of 3.40 V, which was ideal for NRR. The core–shell α-Fe@Fe_3O_4 catalyst was applied in such an IL mixture and

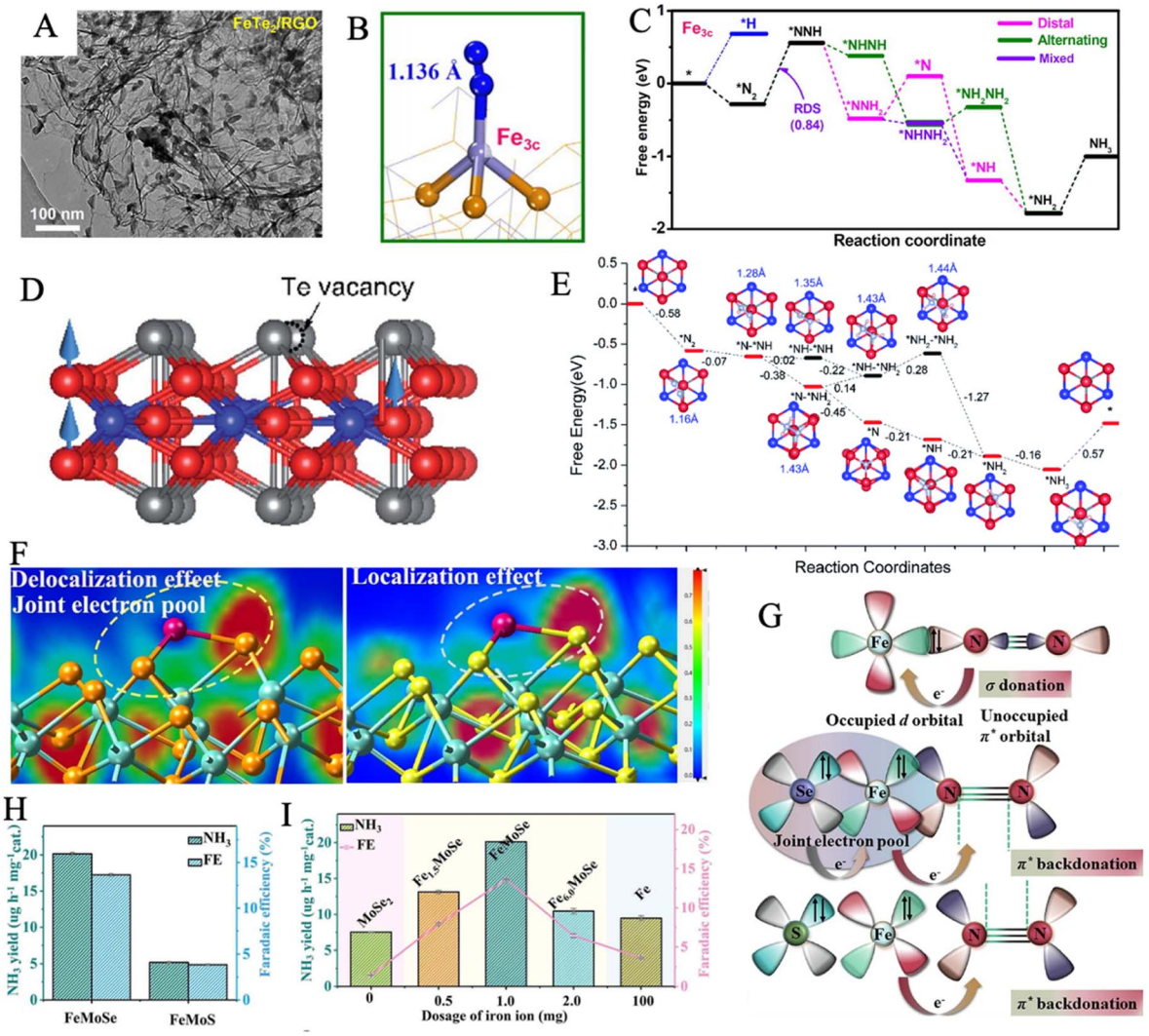

Fig. 5 (A) TEM image of $FeTe_2$/RGO. (B) Optimized structures of $*N_2$ over Fe_{3c} sites. (C) Free energy profiles of three NRR pathways on Fe_{3c} site at $U = 0$. Reproduced with permission: copyright 2021, Elsevier.[129] (D) Side views of the defective Fe_3GeTe_2 monolayer. (color code: red, Fe; bule, Ge; gray, Te) The blue arrows stand for local magnetic moments of Fe atoms up aligned. (E) Possible reaction pathways for NRR. Reproduced with permission: copyright 2021, Royal Society of Chemistry.[130] (F) Electron location function of FeMoSe (left), FeMoS (right), in which the Fe, Mo, Se and S atoms are denoted by red, green, yellow and cyan balls, respectively. (G) Schematic illustration for N_2 binding to FeMoSe and FeMoS. NH_3 yields and FEs of FeMoSe, FeMoS (H) and other comparative samples (I).[132]

accomplished an ammonia yield rate of $\sim 2.35 \times 10^{-11}$ mol s^{-1} cm_{ECSA}^{-2} and NRR selectivity of ~32%.

Thus far, most reported studies of iron oxide catalysts also focused on Fe_2O_3.[100] High-index facets are usually represented by a set of Miller indices {*hkl*} with at least one index greater than 1. These facets have a high density of exposed low-coordination atoms and are therefore more open and active than the tightly packed {111} and {100} low-index facets.[108] The energy barrier of HER can be elevated at some specific HIFs, while a more feasible NRR pathway is opened to improve NRR selectivity.[109] Xie *et al.* combined the facet modulation and nanoarray structure design to improve the NRR performance of α-Fe_2O_3.[110] The α-Fe_2O_3 nanorod arrays (NAs) with exposed (104) HIF offered abundant unsaturated Fe atomic dangling bonds as the NRR active sites. Moreover, the nanoarray structure achieved an enhanced electrochemical surface area (ECSA) to fully display the active sites and maintain sufficient mass diffusion. Thus, the selectively exposed (104) surface coupled with the high ECSA of the nanoarray structure achieves the superior electrocatalytic performance of α-Fe_2O_3 NAs. Unfortunately, current studies on HIFs to optimize the electrocatalytic selectivity and activity are popular in noble metal-based materials and their alloys, such as Pt and Au.[87,111,112] The lattice facets control engineering on iron materials still needs to be explored.

Given the fact that adjusting the OV concentration is an effective method for improving the oxide catalyst properties for NRR, various strategies have been applied for this target, such as annealing and heteroatom doping. High-temperature annealing is a feasible way to increase the concentration of OVs. Cui *et al.* reported an *o*-Fe_2O_3–Ar/CNT catalyst that was

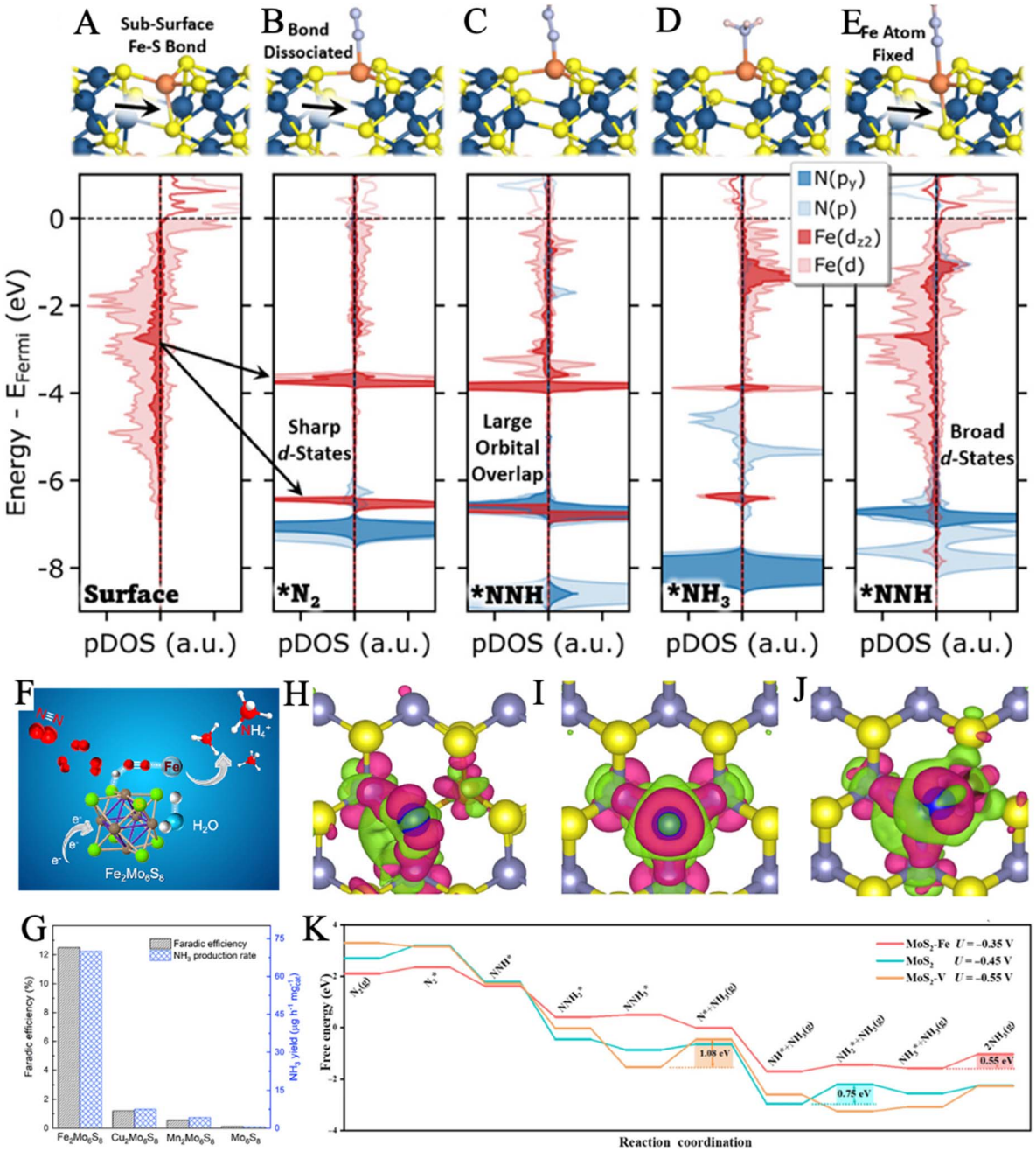

Fig. 6 Structure and projected density of states (pDOS) for the clean $Fe_2Mo_6S_8$ surface (A), the $Fe_2Mo_6S_8$ surface with $*N_2$ (B), *NNH (C), $*NH_3$ (D), and *NNH (E) with the Fe surface atom fixed at its position on the clean surface. Reproduced with permission: copyright 2022, American Chemical Society.[136] (F) Illustration of the proposed binding patterns for N_2 absorption and subsequential conversion to NH_3. (G) Comparison of FE and NH_3 yield for Mo_6S_8 and $M_2Mo_6S_8$ (M = Fe, Mn, and Cu) electrocatalysts. Reproduced with permission: copyright 2021, American Chemical Society.[137] (H–J) Charge density difference of MoS_2–Fe, MoS_2, MoS_2–V (from left to right). Electron excess and deficiency are denoted by red and green isosurfaces, respectively. Isosurface was set as 0.003 $Å^{-3}$. (K) Free-energy profiles of the NRR of MoS_2–Fe, MoS_2, and MoS_2–V. Reproduced with permission: copyright 2022, reproduced with permission: copyright 2021, Springer.[140]

annealed under argon (Ar) utilizing commercial hematite nanopowder as raw material.[44] It was found that the NRR performance of *o*-Fe_2O_3–Ar with the highest OV concentration (12.26%) was better than that of *o*-Fe_2O_3-air and Fe_2O_3-untreated. After 16 hours of the chronoamperometry test, the NH_3 production rate and FE decreased significantly, suggesting that the stability of the structure needs to be improved. However, high-temperature annealing is an energy-intensive process, which is typically carried out in a reducing atmosphere. Thus, the introduction of OVs by doping with low valence metals is highly desirable to be developed as a relatively environmentally friendly synthesis method. Yu *et al.* developed zinc-doped Fe_2O_3 nanoparticles *via* a wet chemical route at only 160 °C.[113] Zinc has a similar ion radius to that of Fe^{3+}, which is

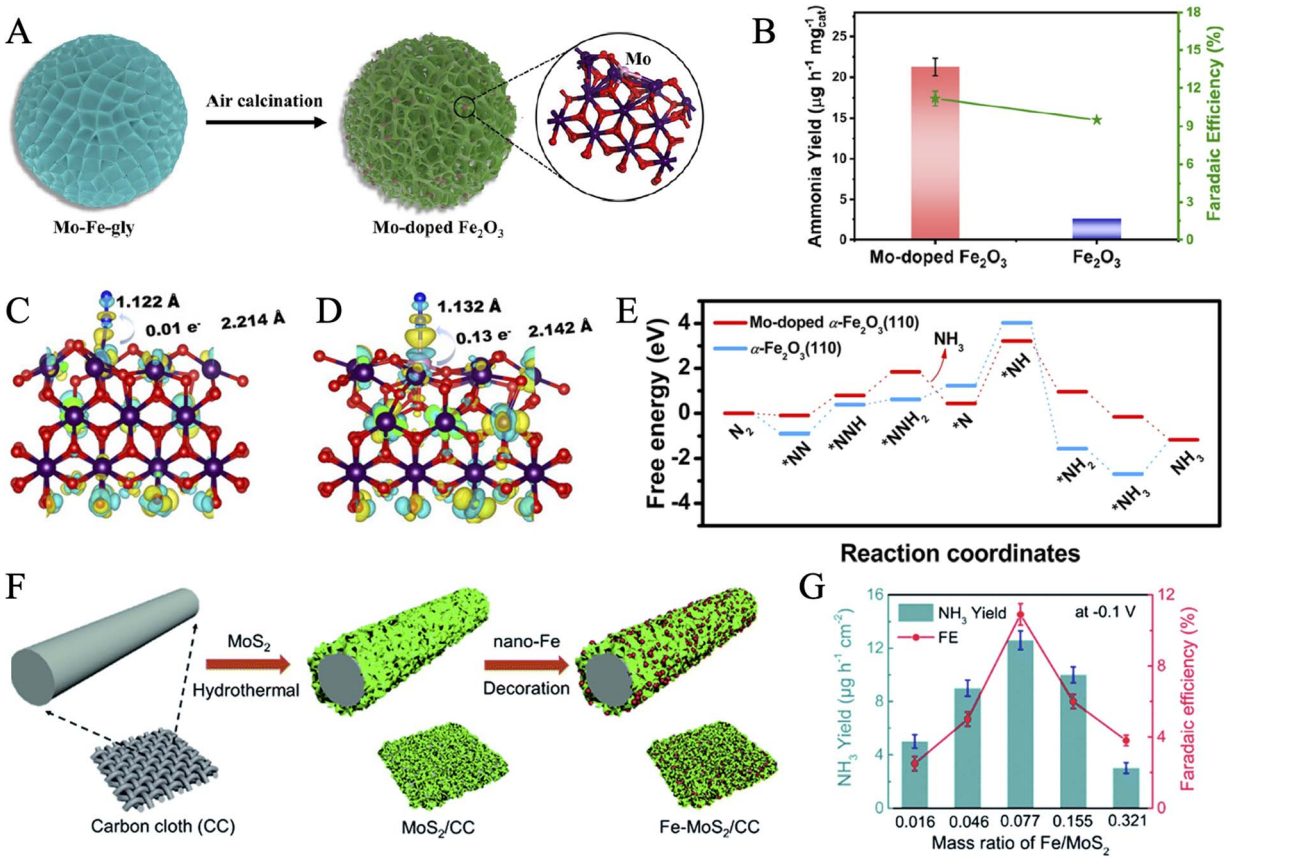

Fig. 7 (A) Diagrammatic representation of the formation of Mo-doped Fe_2O_3 porous nanospheres. (B) Comparison of NH_3 production rates and FEs at −0.6 V for Mo-doped Fe_2O_3 and Fe_2O_3. The charge density difference of N_2-adsorbed α-Fe_2O_3(110) (C) and Mo-doped α-Fe_2O_3(110) (D) with an isosurface value of 0.006 e Å^{-3}. (E) Free energy diagram for the NRR process on α-Fe_2O_3(110) and Mo-doped α-Fe_2O_3(110), respectively. Reproduced with permission: copyright 2022, American Chemical Society.[143] (F) Schematic illustration for the formation routes of Fe–MoS_2/CC. (G) NH_3 yield and FE with different mass ratios of Fe–MoS_2. Loading mass: 2.15 mg cm^{-2}. Reproduced with permission: copyright 2019, Royal Society of Chemistry.[152]

able to induce OVs in Fe_2O_3 nanoparticles. In neutral media, it offers a maximum FE of 10.4% and an NH_3 formation rate of 15.1 μg h^{-1} mg$_{cat}^{-1}$ at −0.5 V *vs.* RHE. Furthermore, Zhang *et al.* were the first to propose a task-specific ionic liquid strategy for OV-rich α-Fe_2O_3 nanocubes (denoted as Fe_2O_3-IL), achieving an NH_3 production rate of 32.13 μg h^{-1} mg$_{cat}^{-1}$ with a FE of 6.63% at 0.3 V *vs.* RHE.[114] The ionic liquid *n*-octylammonium formate (OAF) simultaneously worked as the reaction medium and structure-directing template for growing α-Fe_2O_3 nanocubes while the reductant formic anion of ionic liquid drove rich OVs *in situ* in α-Fe_2O_3. This innovative approach allows the OV concentration to be adjusted under mild conditions. Additionally, the low surface tensions of OAF compared with water resulted in a higher nucleation rate of Fe_2O_3, than the growth rate. Consequently, Fe_2O_3-IL had a much smaller particle size of 23.2 ± 1.8 nm than that of Fe_2O_3 synthesized in a water medium. As a result, a larger specific surface area and more active sites were delivered in the catalytic process.

Most of the catalysts we mentioned above were prepared with the additive of surfactants through solution methods. However, the surfactants had a passivation effect on the catalyst surface, which decreased the activity of the catalyst. Therefore, developing a strategy to construct a clean surface could be critical for achieving high activity.[115] Herein, Wang *et al.* reported porous Fe_2O_3 nanorods grown on carbon cloth (p-Fe_2O_3/CC).[116] The EDX element mapping image suggested that Fe and O elements with a ratio of about 2/3 are uniformly distributed throughout the nanorods. With the assistance of Na_2SO_4 as a structure-directing agent, the self-supported structure of *p*-Fe_2O_3/CC with a large surface area provided abundant active sites and accessible channels for promoting mass/charge transfer during the NRR process. Furthermore, Wang *et al.* successfully synthesized clean-surface Fe_2O_3 nanoparticles without any surfactants or structure-directing agents.[115] $Fe(NO_3)_3$ was dispersed in glycerine for prior hydrothermal treatment, followed by high-temperature calcination. This clean-surface catalyst exhibited better performance with a high yield of NH_3 22 μg h^{-1} mg$_{cat}^{-1}$ and a FE of 3.5% at −0.5 V *vs.* RHE. The as-synthesized catalyst showed good catalytic and structural stability even without a binder.

The conventional preparation of iron oxide materials mostly requires high-temperature annealing, which is not convenient and highly energy intensive. Preparation strategies at room temperature need more exploration. In addition, iron oxide

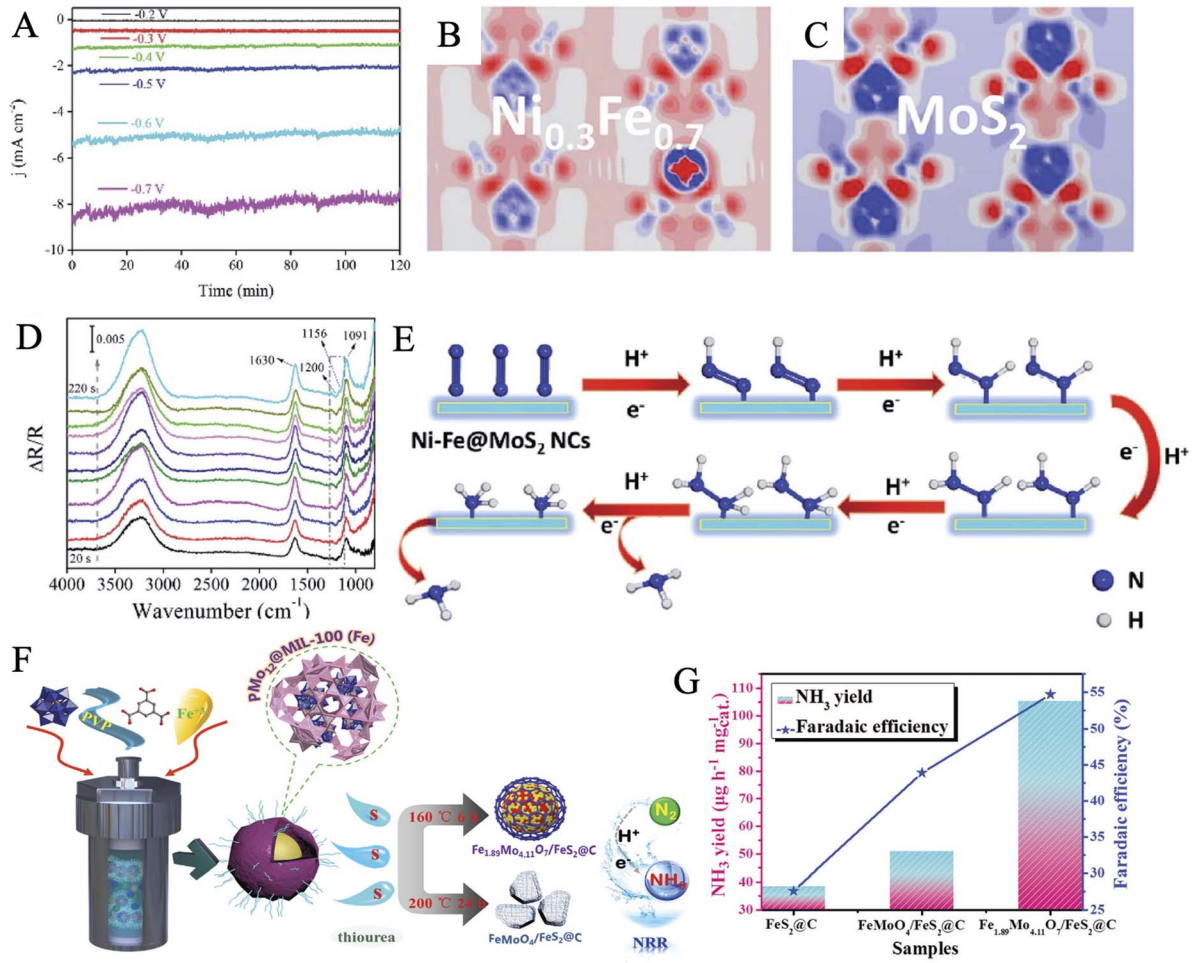

Fig. 8 (A) Time-dependent current density (*j*) of Ni–Fe–MoS_2 at various potentials. Electron density difference of the optimized structures of MoS_2 (B) and $Ni_{0.3}$–$Fe_{0.7}$@MoS_2 (C) (electron excess and deficiency are denoted by red and blue, respectively). (D) *In situ* electrochemical-FTIR spectra of the NRR process on the Ni–Fe–MoS_2 NCs catalyst. (E) Proposed electrocatalytic mechanism on Ni–Fe@MoS_2. Reproduced with permission: copyright 2020, Royal Society of Chemistry.[171] (F) Schematic diagram of the preparation routes of $Fe_{1.89}Mo_{4.11}O_7/FeS_2$@C and $FeMoO_4/FeS_2$@C composites. (G) Comparison of NH_3 production rate and FE of FeS_2@C, $FeMoO_4$@FeS_2@C, and $Fe_{1.89}Mo_{4.11}O_7$@FeS_2@C (1.6 wt%) at the optimum voltage, respectively. Reproduced with permission: copyright 2020, Royal Society of Chemistry.[55]

suffers from poor electrical conductivity, which is against the high catalytic efficiency. Good electron donors can be introduced to modulate the electronic structure of the catalyst. Many of the current iron oxide electrocatalysts for NRR struggle with low ammonia yields or FEs. Further theoretical studies are recommended to explore their catalytic intrinsic principles and thus guide the catalyst improvement.

3.2 Iron chalcogenides

3.2.1 Iron sulfide. S is one of the most important elements in the structure and composition of natural nitrogenase, which is primarily in the form of metal–S units. Metal sulfides have proven to have great potential for clean electrocatalytic nitrogen fixation.[2,117–120] As mentioned above, Fe is the basic entity in FeMo, FeFe, and FeV nitrogenases, providing some insight into the design of NRR catalysts. The typical Fe_4S_4 clusters, which are found in these nitrogenases as electron transfer carriers for reducing N_2, further highlight the significance of iron sulfide complexes for ammonia synthesis.[121] Suitable two-dimensional (2D) iron sulfide has a unique layered structure with extraordinary electrochemical properties and strong anisotropy, which can be used as a platform for hosting active sites.[52] In addition, pyrite (FeS_2) is the most common sulfide mineral on earth, being conducive to economically viable large-scale industrial production.[122] Zhao *et al.* reported an impressive catalyst of NRR based on DES (polyethylene glycol-200/thiourea)-derived Fe_3S_4 nanosheets *via* a one-step solvothermal synthesis (Fig. 4A).[123] The crumpled and mesoporous structure might be formed due to the shape control of surfactant, which is favorable for fast ion/molecule transports. The Fe_3S_4 nanosheets presented a novel NH_3 yield rate of 75.4 μg h^{-1} mg_{cat}^{-1} in 0.1 M HCl at −0.4 V, much better than those of CoS_2 and NiS_2 prepared by the same method, highlighting the importance of iron element for the NRR. Xiong *et al.* reported a self-supportive iron sulfide (FeS_x) NRR electrocatalyst.[124] The H_2S-plasma treatment sulfurized the Fe surface to afford the self-supportive FeS_x layer on

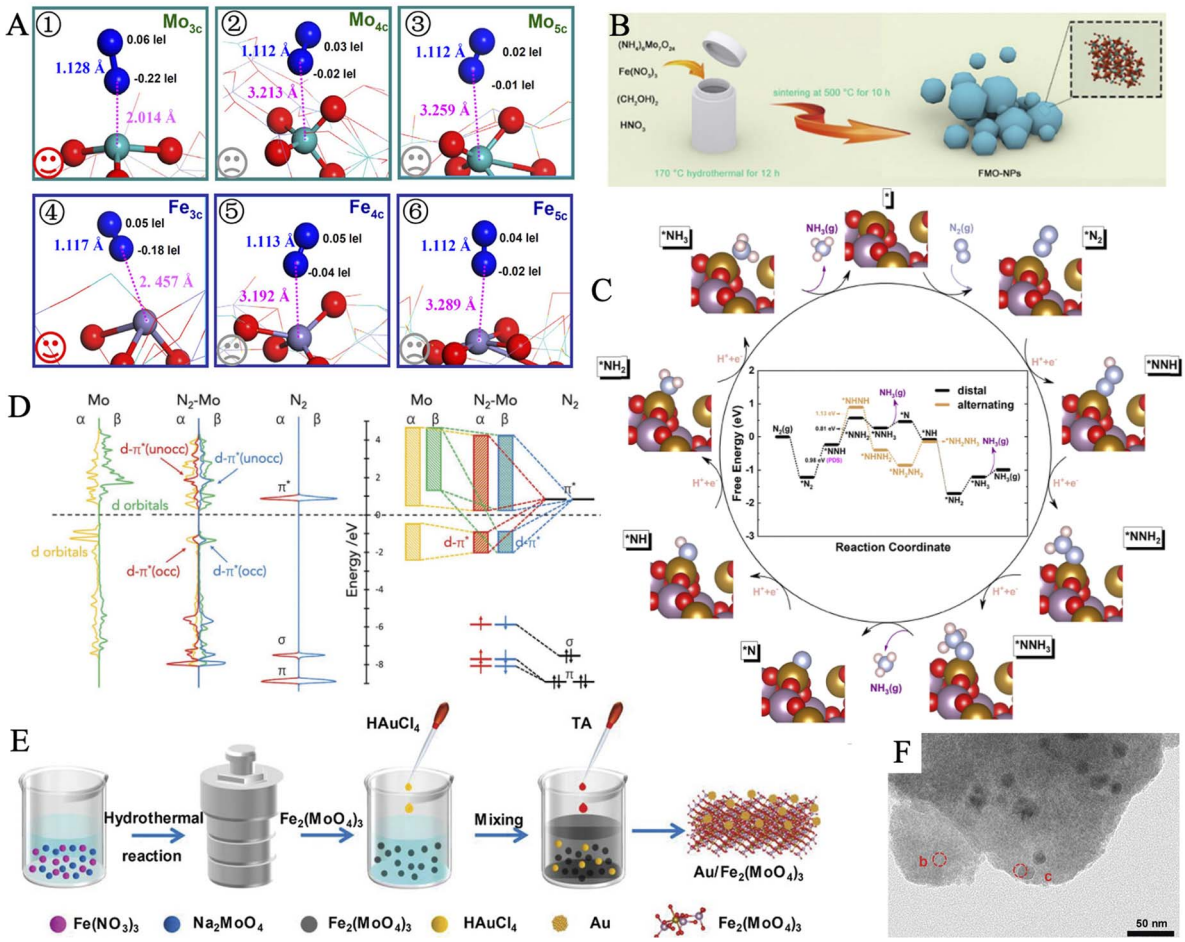

Fig. 9 (A) Optimized structures for N_2 adsorption on various types of Fe and Mo atoms. Reproduced with permission: copyright 2020, American Chemical Society.[175] (B) Schematic illustration of the synthesis for FMO-NPs. (C) Variation of free energy for the distal and alternating pathways at the $Fe_2(MoO_4)_3$ (110) surface. Reproduced with permission: copyright 2020, American Chemical Society.[176] (D) The p-DOS and schematic illustrations of 4d orbitals of Mo atoms on Au/$Fe_2(MoO_4)_3$, 2p-orbitals of the N_2 gas molecule, and their interaction within N_2^*-Au/$Fe_2(MoO_4)_3$. (E) Synthetic route of Au/$Fe_2(MoO_4)_3$. (F) TEM image of Au/$Fe_2(MoO_4)_3$. Reproduced with permission: copyright 2021, Wiley-VCH.[178]

the Fe foam (FeS_x/Fe), which exhibited a high NH_3 yield rate of 4.13×10^{-10} mol s^{-1} cm^{-2} and a FE of 17.6%. The FeS_x/Fe electrocatalyst demonstrated excellent stability, with a negligible decrease in current density after 20 h of electrolysis.

Inducing surface defects is an available strategy to increase the active sites of NRR *via* heteroatom doping. In a recent work, a surface-defective FeS_2 catalyst was obtained by sulfurization of stainless-steel foil at 500 °C.[125] The fitting of the XPS spectrum sulfur S 2p peaks and the HRTEM image proved the existence of abundant SVs. Meanwhile, such defects were considered to be the active sites for the stable and efficient adsorption of dinitrogen molecules. It was strongly advised that the generation of an active hydrogen atom was primarily caused by the exposed (210) facet of iron pyrite. The stainless-steel-based catalyst possessed a considerably higher FE of 14.6% in contrast to the pure iron-based catalyst in 0.1 M Li_2SO_4 at −0.2 V. Because of the existence of Cr species, the SS-based electrode with anti-corrosion properties presented a superior catalytic stability under acidic conditions. Hou *et al.* reported a porous exfoliated $FePS_3$ nanosheet with rich SVs (Vs-FePS3 NSs), which was formed through electrochemical exfoliation and hydrogenation.[52] Vs-$FePS_3$ NSs showed significant activity in the electrocatalytic NRR with a high NH_3 yield rate of 3.88 μg h^{-1} cm^{-2} at −0.25 V and a FE of 12.36% at −0.20 V *versus* RHE due to their rich SV and unique 2D morphology. To identify the actual active sites of Vs-$FePS_3$ NSs for NRR, SCN^- ion was used to act as a poisoning reagent for metal-centered active sites. A significant decrease appeared in the current density and FE (from 12.36% to 5.31%), indicating that the active Fe site was effectively shielded (Fig. 4B). The shift of S 2p main peaks to higher binding energies in high-resolution XPS spectra suggested that the SVs boosted the hydrogenation of N_2 (Fig. 4C).

The suitable ligand configuration of the active sites plays a significant role in enhancing the catalytic performance. It is found that a metal sulfur cluster with four permanent ligands in a twisted tetrahedral ligation shell is an effective active center of NRR. This coordination structure is well demonstrated in FeS_2, where the NRR process proceeds preferably on Fe atoms (Fig. 4D). In a recent study, a FeS_2 NRR catalyst was synthesized *via* the one-step hydrothermal method.[126] The catalyst exhibited

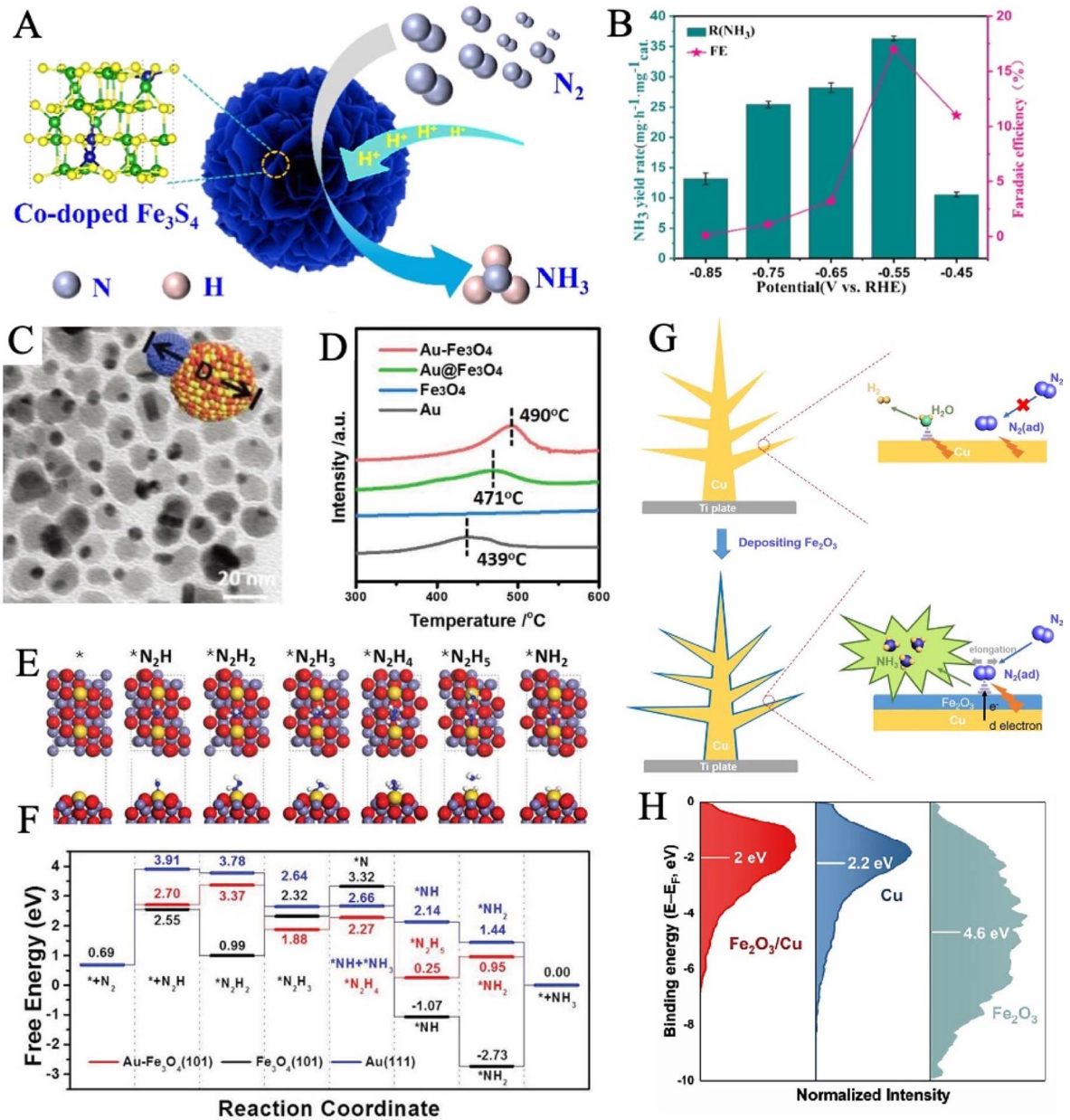

Fig. 10 (A) Schematic of Co-doped Fe_3S_4 nanoflowers. (B) NH_3 yields and FEs of Co-doped Fe_3S_4 nanoflowers at a series of applied potentials. Reproduced with permission: copyright 2020, American Chemical Society.[185] (C) TEM image of Au–Fe_3O_4 NPs. (D) N_2 temperature-programmed desorption curves of different catalysts. (E) The geometric structure of various intermediate states during NRR, in which the hydrogen, oxygen, nitrogen, iron, and gold atoms are denoted by white, red, blue, slate blue, and yellow balls, respectively. (F) Free energy diagram of the NRR pathways on Au–Fe_3O_4 (101), Fe_3O_4 (101), and Au (111). Reproduced with permission: copyright 2020, Wiley-VCH[184] (G) Illustration of synthesis and electronic interactions of dendritic Fe_2O_3/Cu electrocatalyst. (H) XPS valence band spectra of Fe_2O_3/Cu, Cu, and Fe_2O_3. Reproduced with permission: copyright 2019, Elsevier.[186]

an outstanding NRR performance, achieving a high NH_3 yield rate of 37.2 μg h^{-1} mg$_{cat}^{-1}$ and a FE of 11.2% at −0.5 V *versus* RHE. The current density and original structure of FeS_2 had no significant change after 12 h of electrolysis, indicating excellent durability and stability. Fe atoms were proven to be the active sites instead of S atoms by poisoning experiments and free energy profile for NRR in Fe sites and S sites. The reaction mechanism was investigated by DFT calculations that showed that the associative distal pathway was preferred and the conversion from *NH_2 to *NH_3 was regarded as the potential-determining step (PDS) (Fig. 4E).

The heterostructure of iron sulfide-based catalysts has also been developed to enhance their catalytic performance. The interface within heterostructures can usually regulate the electronic structure and expose extra active sites simultaneously. Chen and coworkers designed a hybrid catalyst of crystalline Fe_2O_3 with amorphous FeS (Fe_2O_3/FeS) *via* a DES-regulated fabrication, followed by an annealing process.[127] The hybrid

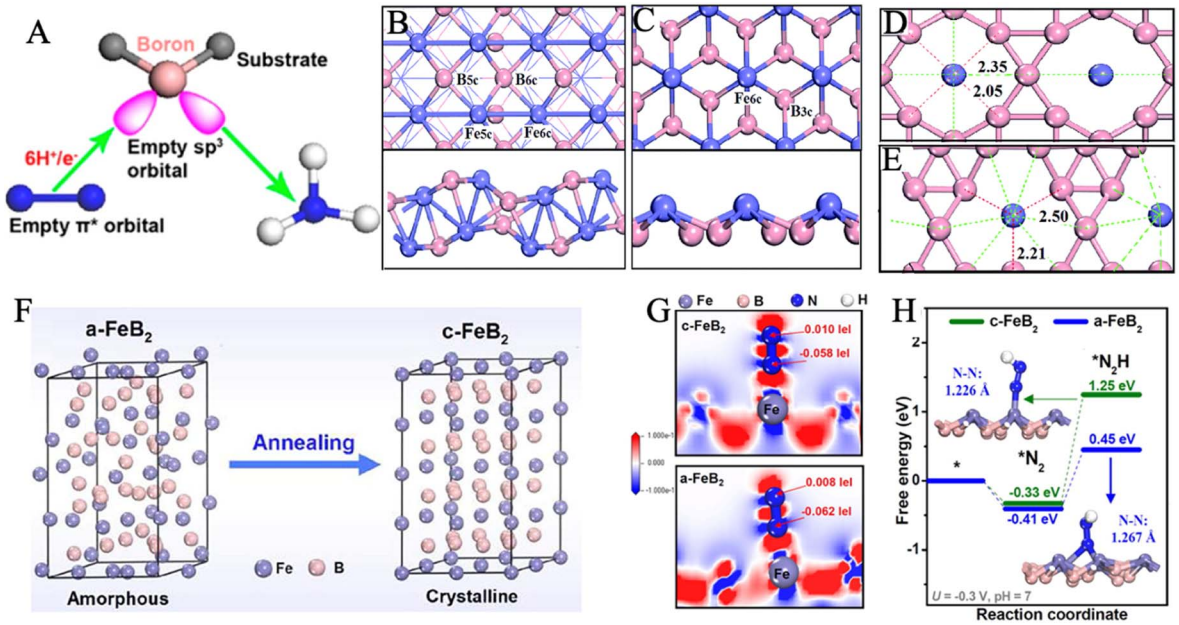

Fig. 11 (A) Schematic of π-backdonation between boron and N_2. Reproduced with permission: copyright 2019, American Chemical Society.[192] Top and side views of FeB (B) and FeB_2 (C). Fe and B are represented as purple and pink balls, respectively. Models and bonding network for (D) FeB_6 (α) and (E) FeB_6 (β). The length of Fe–B_{5c} (short) and Fe–B_{6c} (long) bonds are labeled in units of Å. Reproduced with permission: copyright 2019, Royal Society of Chemistry.[58] (F) Illustration of the phase transformation from a-FeB_2 to c-FeB_2. (G) Charge density difference: the electron accumulation and depletion are represented as red and blue regions, respectively. (H) Free energy profiles of *N_2 and *N_2H adsorption on c-FeB_2 and a-FeB_2. Reproduced with permission: copyright 2021, Elsevier.[57]

catalyst exhibited abundant channels and a high specific surface area of up to 103.94 $m^2\ g^{-1}$, providing more exposed electrochemical active sites for N_2 fixation and accelerating mass convection. Interface engineering between crystalline Fe_2O_3 and amorphous FeS optimized electron distribution and surface structure, being conducive to the absorption and activation of the N_2 molecules. In another work, Gao *et al.* created a graphene oxide-wrapped pyrite nanoparticle (FeS_2@GO) *via* $Fe(NO)_3$, $NH_3 \cdot H_2O$, and graphene oxide as a precursor.[128] The coupling effect between the catalyst and the substrate accelerated the electron transport property, FeS_2@GO exhibited the smallest charge transfer resistance, highest NH_3 production, and FE, much better than those of pure FeS_2 and GO (Fig. 4F and G). Meanwhile, the NH_3 yield rate and FE remained almost constant during the six-time recycling tests (Fig. 4H). Importantly, the low-coordinated Fe atoms are activated as highly active sites, where the free energy change ΔG (*N_2) of N_2 binding was reduced to −0.57 V, leading to stronger binding of N_2 and longer N≡N bond of absorbed *N_2 with respect to pristine FeS_2 (100).

Further progress in iron sulfide can be made by modulating the electronic structures of electrocatalysts by doping, tailoring surface vacancies, defect engineering, and/or heterointerface engineering. Meanwhile, refining and creating more active sites are also proposed to optimize the adsorption and activation of the nitrogen species.

3.2.2 Iron selenide/iron telluride. Other chalcogenides with similar properties to sulfur have also been studied for developing iron-based catalysts. In contrast to metal oxides and sulfides, metal tellurides with metallic properties are emerging as a promising class of electrocatalysts, due to their good electrical conductivity for favorable electrochemical kinetics. Guo and coworkers supported $FeTe_2$ nanoparticles on reduced graphene oxide to form a hybrid ($FeTe_2$/RGO) (Fig. 5A), which performed a novel NRR activity with ammonia yield of 39.2 μg $h^{-1}\ mg_{cat}^{-1}$ and a FE of 18.1%.[129] The 3-fold coordinated Fe (Fe_{3c}) sites acted as the NRR active centers of $FeTe_2$, which could absorb the N_2 molecule and inject −0.12*e* to *N_2 to elongate the N≡N triple bond to 1.136 Å (Fig. 5B). According to the Gibbs free energy diagrams, the mixed pathway is the most favored reaction route. In addition, the $FeTe_2$ effectively suppressed HER, *via* a highly positive adsorption-free energy of *H of 0.71 eV compared to the negative ΔG_{*N_2} of −0.27 eV (Fig. 5C). 2D ferromagnetic materials with large spin moments are newly discovered as high-performance NRR electrocatalysts. In theory, the Fe_3GeTe_2 monolayer was explored as an NRR electrocatalyst through DFT calculations.[130] The highly centralized spin-polarization on the exposed Fe_4 center in defective Fe_3GeTe_2 with TeVs contributed to strong π^*_{2p} back-donation and effective activation of the N≡N triple bond (Fig. 5D). Importantly, an enzymatic pathway is preferred, and all six hydrogenation steps are exothermic and thus spontaneous, during the NRR process ($N_2 + 6H^+ + 6e^- = 2NH_3$) (Fig. 5E). HER can also be suppressed by the rapid termination of N_2 molecules on TeVs.

2D layered double hydroxide (LDH) with evenly distributed ferric ions exhibited N_2 fixation activity, but the intrinsic resistivity and poor charge transfer properties astricted its further application. A NiFe-LDH-derived NiFe-selenide ($Ni_{0.75}Fe_{0.25}Se_2$)

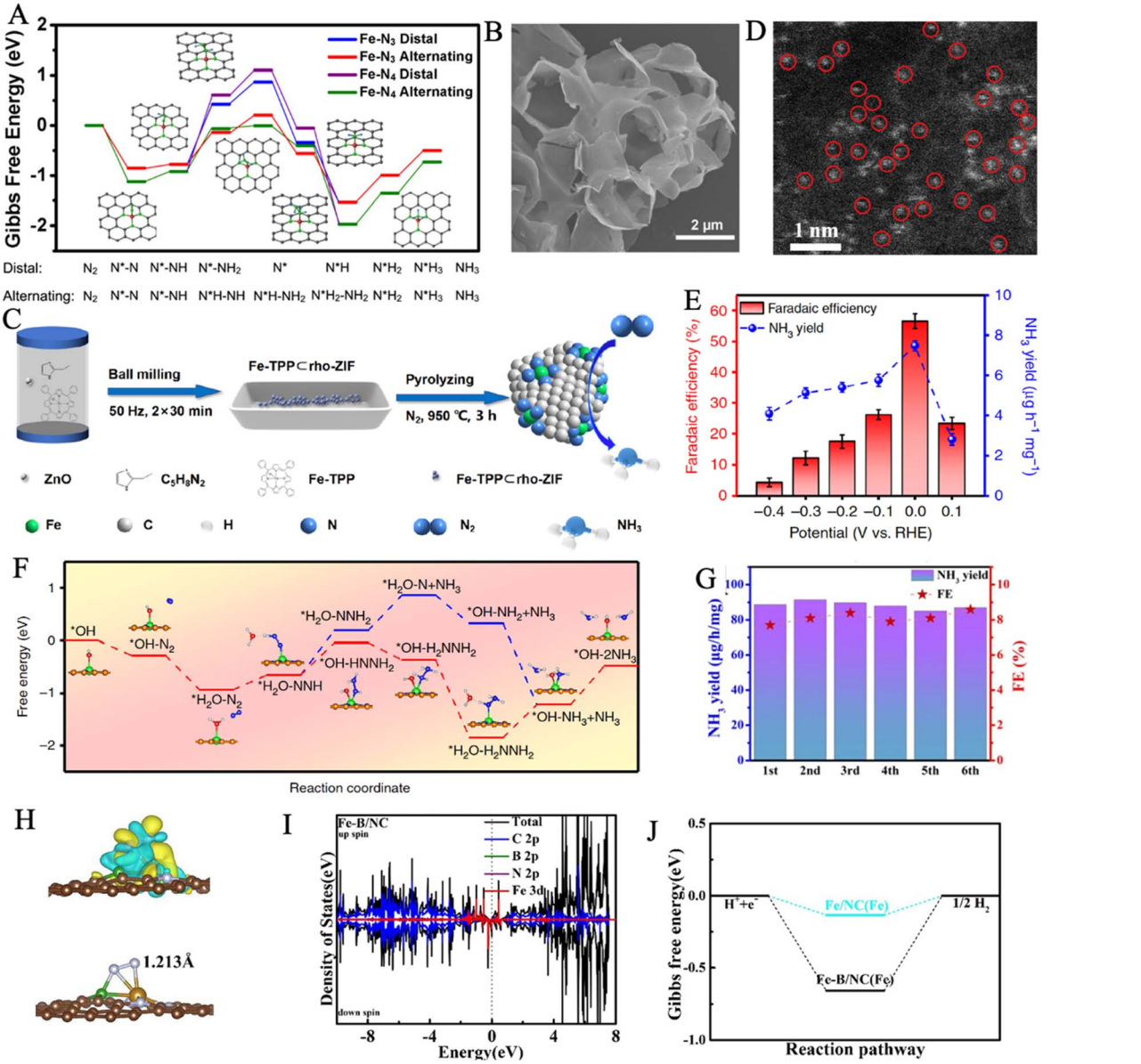

Fig. 12 (A) Gibbs free energy profiles of NRR on Fe–N_3 and Fe–N_4 through alternating and distal pathways. The inset shows the optimized structure of Fe–N_3 coordination and the corresponding adsorption of the NRR intermediates. Reproduced with permission: copyright 2020, American Chemical Society.[210] (B) SEM images of carbon substrate. Reproduced with permission: copyright 2019, American Chemical Society.[216] (C) Schematic illustration of the synthesis routes of Fe–N/C-CPs. (D) HAADF-STEM image and magnified image of Fe–N/C. The Fe-SA centers are marked by red circles. Reproduced with permission: copyright 2021, American Chemical Society.[213] (E) NH_3 yield rates and FEs at each given potential of FeSA–N–C. (F) Free energy profiles for NRR on the FeSA–N–C catalyst at $U = 0$ V. The inset represents the corresponding adsorption models (H, C, N, O, and Fe atoms are represented with gray, orange, blue, red and green spheres, respectively). Reproduced with permission: copyright 2019, Springer.[218] (G) NH_3 yields and FEs during six-recycling tests at −0.45 V *vs.* RHE. (H) Charge density difference and the N–N bond length after N_2 adsorption (I) The density of states for C 2p, B 2p, N 2p and Fe 3d for Fe–B/NC. (J) Gibbs free energy profiles of the H_2 evolution on the as-prepared sample. Reproduced with permission: copyright 2022, Elsevier.[222]

was designed to solve this weakness, the introduction of selenium conspicuously accelerated the p–d coupled electron transfer during nitrogen reduction.[131] Through theoretical analysis, the selenization of iron caused lattice distortion, which may arise from the uneven occupation of t_{2g}^4 and e_g^2 orbitals in Fe^{2+}. More N_2 molecule adsorption sites were introduced by lattice distortion regulation. A bio-inspired joint electron pool was realized in FeMo(Se, Te) by replacing sulfur with selenium or tellurium.[132] Notably, Se and Te had a lower electron-negativity as compared with S, allowing a more expansive electron cloud to form the joint electron pool, which originated from the delocalized electronic structure (Fig. 5F). The density of state (DOS) profiles of the top valence band near the Fermi level in FeMoSe is mainly composed of Fe d, Mo d, and Se p valence orbitals, illustrating a higher electron density and charge transport ability than those of FeMoS and $MoSe_2$.

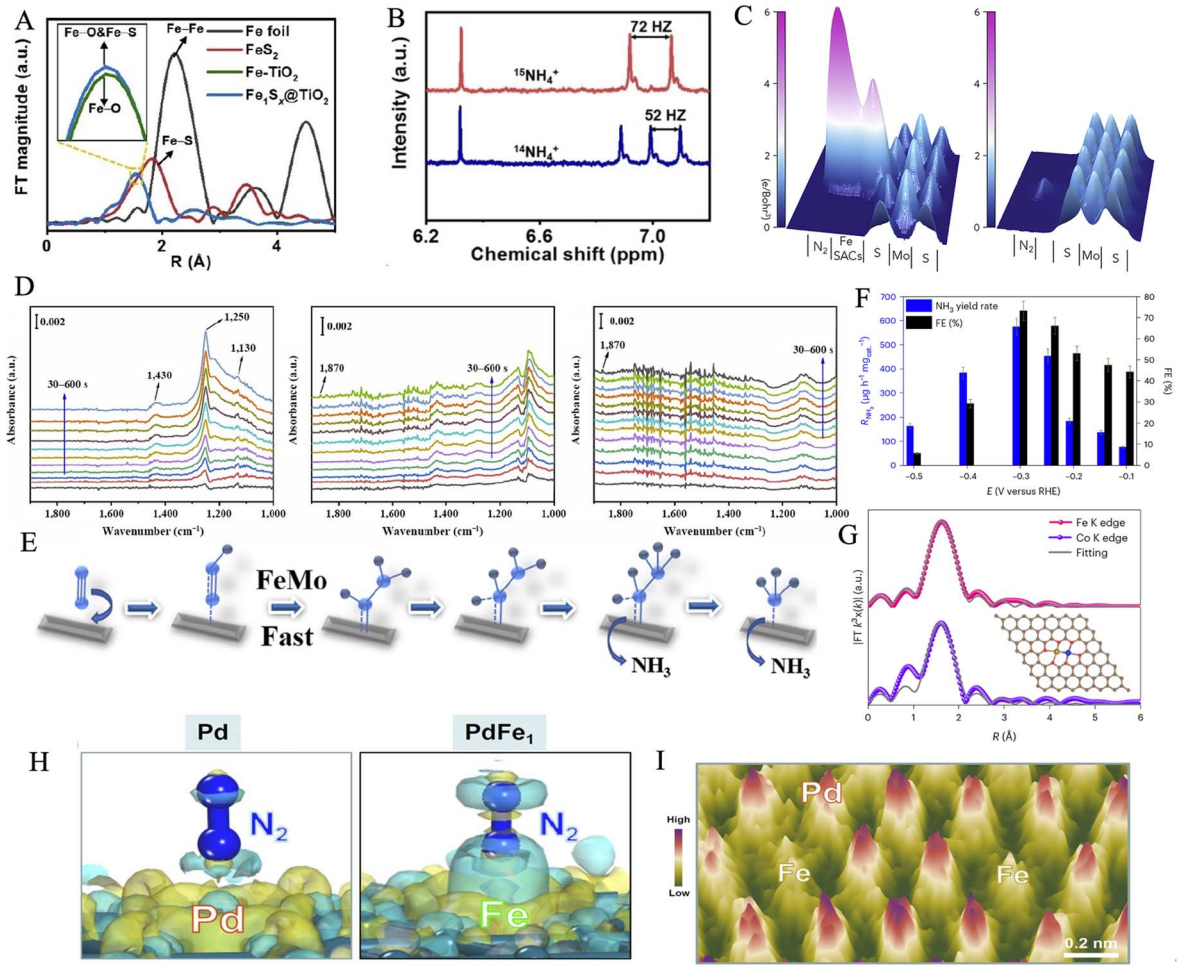

Fig. 13 (A) k^3-weighted Fourier-transform EXAFS spectra of the Fe R-space for FeS_2 and Fe foil, Fe_1S_x@TiO_2 and Fe–TiO_2, the inset is the first peak of Fe_1S_x@TiO_2 and Fe–TiO_2. (B) ^{1}H-NMR spectra of $^{14}NH_4^+$ and $^{15}NH_4^+$ produced in the NRR process. Reproduced with permission: copyright 2022, Wiley-VCH.[60] (C) 3D topographic potential distribution images of MoS_2 and pure MoS_2. Reproduced with permission: copyright 2020, Elsevier.[224] (D) *In situ* FTIR spectra obtained on the surfaces of FeMo/NC, Fe/NC, and Mo/NC SACs, respectively (from left to right). (E) Proposed NRR pathways on FeMo/NC, Fe/NC, and Mo/NC surfaces. Reproduced with permission: copyright 2022, Springer.[231] (F) NH_3 yields and FEs on various applied potentials. (G) Fe and Co K edge EXAFS fitting curves of Fe/Co–O–C-1.0 at R space. Inset is the predicted bimetallic Fe–Co coordination configuration in Fe/Co–O–C-1.0. (C, O, Fe, and Co are denoted by brown, red, orange, and blue, respectively). Reproduced with permission: copyright 2022, Springer.[233] (H) Differential charge densities of absorbed N_2 on Pd and $PdFe_1$, where electron accumulation and depletion are denoted by yellow and cyan, respectively. (I) 3D topographic atom images of $PdFe_1$. Reproduced with permission: copyright 2022, Wiley-VCH.[59]

Theoretical models for the joint electron pool displayed stronger nitrogen adsorption, which is critical for the subsequent hydrogenation steps. As these, FeMoSe had a greater ability to inject electrons into N_2 (Fig. 5G), exhibiting an NH_3 yield rate of 20.14 μg h^{-1} mg_{cat}^{-1} and a FE of 13.65%, which were far better than those of FeMoS and other comparative samples (Fig. 5H and I).

Briefly, the novel metal chalcogenides may be promising electrocatalysts with high efficiency for ammonia synthesis from gaseous dinitrogen. There is a large space for scientists to apply multi-element doping and heterostructure engineering similar to that used in iron sulfides to further promote NRR electrocatalysis. More in-depth research about iron selenide/iron telluride is expected to promote this electrocatalytic NRR field.

3.3 Bimetallic Fe-containing catalysts

3.3.1 Bimetallic Fe–Mo-based catalysts. Based on the structure of Mo,Fe-nitrogenase from natural conditions, Mo–Fe bimetallic catalysts have attracted extensive attention.[101,133–135] Theoretical calculations and experimental works proofed that synergy and electron coupling effect between Fe and Mo facilitate the charge transfer from metal orbitals to nitrogen species, and thus weaken the inert nitrogen triple bond.[56,118,136,137] Singstock *et al.* explored how $Fe_2Mo_6S_8$ broke NRR scaling relationships using grand-canonical density functional theory (GC-DFT).[136] According to theoretical predictions, Mo sites exhibited the intrinsic characteristics of strong N_2 adsorption and large NH_3 dissociation barriers, even poisoning due to the over-binding of $*NH_3$. Fe active sites with sharp bands of free-atom-like d-states conspicuously overlapped with the nitrogen

Table 1 NRR performance of the Fe-based catalysts reported since 2018

Catalyst	Electrolyte	NH_3 yield	Quantification methods	FE (%)	Isotope labeling	Ref.
o-Fe_2O_3–Ar/CNT	0.1 M KOH	0.46 μg h^{-1} cm^{-2}	Nessler colorimetry	6.0	No	44
Fe/Fe_3O_4-300	0.1 M phosphate buffer solution	0.19 μg h^{-1} cm^{-2}	Indophenol blue colorimetry	8.29	No	100
Fe–Fe_3O_4 nanoparticles	0.1 M Na_2SO_4	24.6 μg h^{-1} mg_{cat}^{-1}	Indophenol blue colorimetry	53.2	No	50
Fe_3O_4-300 nanosheet	0.1 M Na_2SO_4	12.09 μg h^{-1} mg_{cat}^{-1}	Indophenol blue colorimetry	34.38	Yes	49
Fe–Fe_3O_4 nanoparticles	0.1 M Na_2SO_4	22 μg h^{-1} mg_{cat}^{-1}	Indophenol blue colorimetry	3.5	No	115
p-Fe_2O_3/CC	0.1 M Na_2SO_4	6.78 μg h^{-1} cm^{-2}	Indophenol blue colorimetry	7.69	No	116
Zn doped Fe_2O_3	0.1 M Na_2SO_4	15.1 μg h^{-1} mg_{cat}^{-1}	Indophenol blue colorimetry	10.4	Yes	113
α-Fe_2O_3 nanocubes	0.1 M KOH	32.13 μg h^{-1} mg_{cat}^{-1}	Indophenol blue colorimetry	6.63	Yes	114
Au–Fe_3O_4 nanoparticles	0.1 M KOH	21.42 μg h^{-1} mg_{cat}^{-1}	Nessler colorimetry	10.54	Yes	184
Fe_2O_3/Cu	0.1 M KOH	15.66 μg h^{-1} mg_{cat}^{-1}	Indophenol blue colorimetry	24.4	No	186
Fe_3S_4 nanosheets	0.1 M HCl	75.4 μg h^{-1} mg_{cat}^{-1}	Indophenol blue colorimetry	6.45	Yes	123
FeS_x/Fe	0.1 M KOH	4.13 × 10^{-10} mol s^{-1} cm^{-2}	Ion chromatography, indophenol blue colorimetry, Nessler colorimetry	17.6	Yes	124
Vs-$FePS_3$ NSs	0.1 M HCl	3.88 μg h^{-1} cm^{-2}	Ion chromatography, indophenol blue colorimetry	12.36	No	52
FeS_2	0.1 M Na_2SO_4	37.2 μg h^{-1} mg_{cat}^{-1}	Indophenol blue colorimetry	11.2	No	126
FeS_2	0.1 M Li_2SO_4	11.5 μg h^{-1} mg_{Fe}^{-1}	Nessler colorimetry	14.6	No	125
Fe_2O_3/FeS	0.1 M KOH	34.31 μg h^{-1} mg_{cat}^{-1}	Indophenol blue colorimetry	18.06	Yes	127
FeS_2@GO	0.1 M HCl & 0.1 M Na_2SO_4	78.6 μg h^{-1} mg_{cat}^{-1} in 0.1 M HCl, 27.9 μg h^{-1} mg_{cat}^{-1} in 0.1 M Na_2SO_4	Indophenol blue colorimetry	4.7 in 0.1 M HCl, 6.8 in 0.1 M Na_2SO_4	No	128
$FeTe_2$/RGO	0.5 M $LiClO_4$	39.2 μg h^{-1} mg_{cat}^{-1}	Indophenol blue colorimetry	18.1	Yes	129
FeMoSe	0.1 M Na_2SO_4	20.14 μg h^{-1} mg_{cat}^{-1}	Indophenol blue colorimetry	13.65	Yes	132
FeS_2–Mo	0.1 M KOH	26.15 μg h^{-1} mg_{cat}^{-1}	Indophenol blue colorimetry, Nessler colorimetry, ion chromatography	14.41	Yes	56
$Fe_2Mo_6S_8$	0.5 M Na_2SO_4 mixed with 0.1 M sodium citrate buffer	70 μg h^{-1} mg_{cat}^{-1}	Indophenol blue colorimetry	12.5	Yes	137
MoS_2–Fe	0.1 M Na_2SO_4	20.11 μg h^{-1} mg_{cat}^{-1}	Indophenol blue colorimetry	15.72	No	140
Fe–MoS_2	0.5 M K_2SO_4	8.63 μg h^{-1} mg_{cat}^{-1}	Indophenol blue colorimetry	18.8	Yes	142
Mo-doped Fe_2O_3	0.1 M Na_2SO_4	21.3 μg h^{-1} mg_{cat}^{-1}	Indophenol blue colorimetry	11.2	No	143
MoO_2/FeS_2/GA	0.1 M HCl	40.18 μg h^{-1} mg_{cat}^{-1}	Indophenol blue colorimetry	37.44	Yes	146
FeS@MoS_2/CFC	0.1 M Na_2SO_4	8.45 μg h^{-1} cm^{-2}	Indophenol blue colorimetry	2.96	No	54
Fe–MoS_2/CC	0.1 M KOH	12.5 μg h^{-1} cm^{-2}	Indophenol blue colorimetry	10.8	Yes	152
SACs-MoS_2-Fe	0.1 M KCl	97.5 μg h^{-1} cm^{-2}	Indophenol blue colorimetry	31.6	Yes	224
MoFe-PC	0.1 M HCl	34.23 μg h^{-1} mg_{cat}^{-1}	Indophenol blue colorimetry	16.83	No	170
$Ni_{0.3}$–$Fe_{0.7}$@MoS_2	0.1 M Na_2SO_4	128.17 μg h^{-1} mg_{cat}^{-1}	Indophenol blue colorimetry	11.34	No	171
$Fe_{1.89}Mo_{4.11}O_7$/FeS_2@C	0.5 M K_2SO_4	105.3 μg h^{-1} mg_{cat}^{-1}	Nessler colorimetry	54.7	Yes	55
$FeMoO_4$ nanorods	0.1 M Na_2SO_4	17.51 μg h^{-1} mg_{cat}^{-1}	Indophenol blue colorimetry	10.53	No	174
$FeMoO_4$ nanorods	0.5 M $LiClO_4$	45.8 μg h^{-1} mg_{cat}^{-1}	Indophenol blue colorimetry	13.2	Yes	175
$Fe_2(MoO_4)_3$ nanoparticles	0.1 M Na_2SO_4	18.16 μg h^{-1} mg_{cat}^{-1}	Indophenol blue colorimetry	9.1	No	176
Au/$Fe_2(MoO_4)_3$	0.2 M Na_2SO_4	7.61 μg h^{-1} mg_{cat}^{-1}	^{1}H-NMR method		Yes	178
α-FeB_2 PNS	0.5 M $LiClO_4$	39.8 μg h^{-1} mg_{cat}^{-1}	Indophenol blue colorimetry	16.7	Yes	57
Fe SAC/N–C	0.1 M KOH	53.12 μg h^{-1} mg_{cat}^{-1}	Indophenol blue colorimetry	39.6	Yes	210

Table 1 (*Contd.*)

Catalyst	Electrolyte	NH_3 yield	Quantification methods	FE (%)	Isotope labeling	Ref.
Fe–N/C	0.5 M K_2SO_4	2.27 μg h^{-1} mg_{cat}^{-1}	Indophenol blue colorimetry	7.67	Yes	213
FePc/C	0.1 M Na_2SO_4	137.95 μg h^{-1} mg_{FePc}^{-1} 10.25 μg h^{-1} mg_{cat}^{-1}	Indophenol blue colorimetry	10.05	No	216
FeSA–N–C	0.1 M KOH	7.48 μg h^{-1} mg_{cat}^{-1}	Indophenol blue colorimetry	56.55	Yes	218
Fe–B/NC	0.1 M KOH	88.7 μg h^{-1} mg_{cat}^{-1}	Indophenol blue colorimetry	9.2	Yes	222
Fe_1S_x@TiO_2	0.1 M HCl	18.3 μg h^{-1} mg_{cat}^{-1}	Indophenol blue colorimetry	17.3	Yes	60
FeMo/NC DSACs	0.1 M Na_2SO_4	26.8 μg h^{-1} mg_{cat}^{-1}	Indophenol blue colorimetry	11.8	No	231
Fe/Co–O–C-*r*	0.1 M Na_2SO_4	579 μg h^{-1} mg_{cat}^{-1}	Indophenol blue colorimetry, ^{1}H-NMR method	79.0	Yes	233
$PdFe_1$	0.5 M $LiClO_4$	111.9 μg h^{-1} mg_{cat}^{-1}	Indophenol blue colorimetry	37.8	Yes	59

p-states of *NNH, instead of those of $*N_2$ or $*NH_3$ (Fig. 6A–E), stabilizing the key *NNH intermediates and ensuring smooth release of NH_3. Experiments well supported the above idea, and further revealed the principle of HER inhibition effect.[137] During the catalysis process, Fe/Mo sites effectively absorbed and activated N_2 molecules. Then, the ligand effect where Fe donated electrons to Mo_6S_8 strengthened this HER-suppressed effect. This work also unraveled the multisite functions: Fe/Mo sites for N_2 adsorption and activation, and S sites for *H intermediate stabilization. Moreover, synergistic multisites of Fe, Mo, and S in the $Fe_2Mo_6S_8$ optimized the reactive energy of the intermediates and concurrently depressed hydrogen evolution, to achieve higher selectivity and yield of ammonia (Fig. 6F and G). Reasonable design of Mo–Fe bimetallic catalysts can be realized by heteroatom doping, interface engineering, single

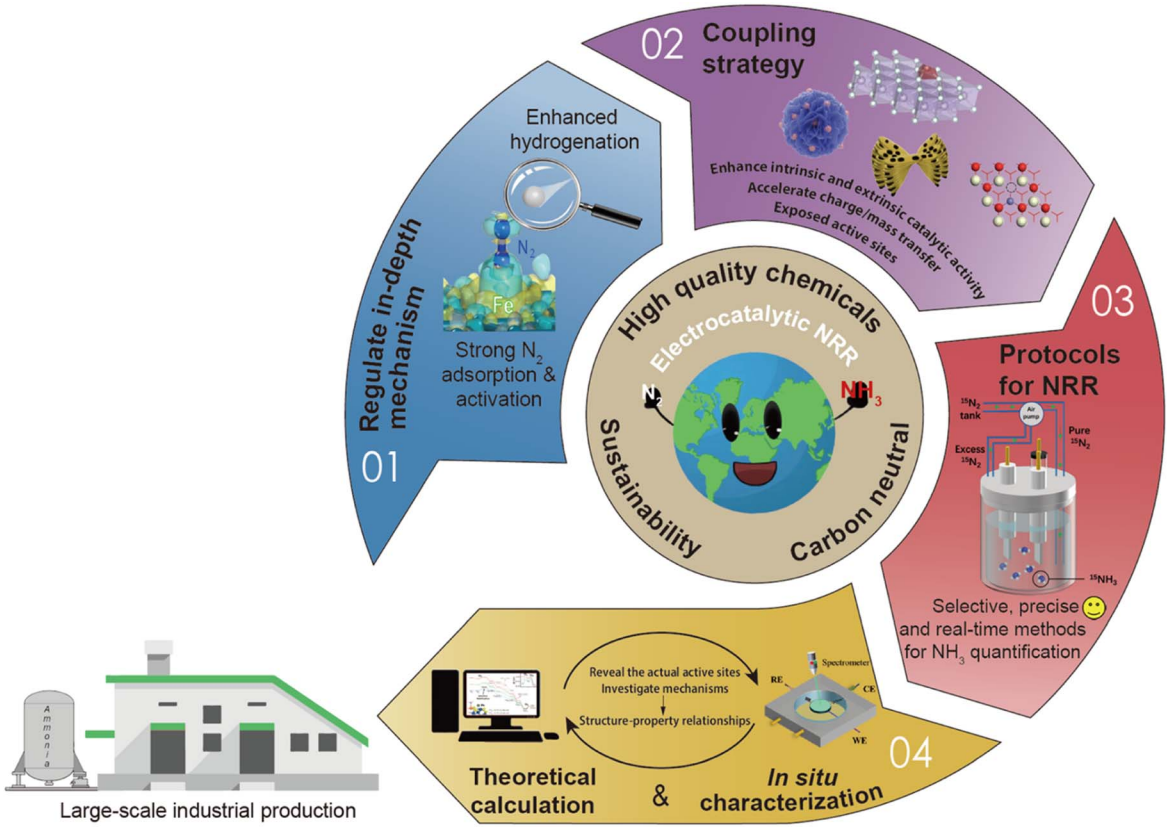

Fig. 14 Strategies to boost NRR performances and perspectives for future developments of iron-based catalysts. Regulate in-depth mechanism: reproduced with permission: copyright 2022, Wiley-VCH.[59] Coupling strategy: reproduced with permission: copyright 2020, Royal Society of Chemistry.[237] Copyright 2022, Elsevier.[150] Copyright 2020, Elsevier.[224] Theoretical calculation: reproduced with permission: copyright 2022, American Chemical Society.[136]

atom dispersion, and metal–organic framework precursors design; the related progress will be discussed in this section.

3.3.1.1. Heteroatom doping. Single Fe-based or Mo-based catalysts can be mutually doped to achieve better N_2 fixation performance by modifying their intrinsic nature. MoS_2 was recently indicated to be a potential material for NRR, as its sufficient Mo (at IV valence states) active sites are able to accept the electrons from N_2.[6,56,79] Nevertheless, its further application is limited by the strong adsorption capacity of Mo to N_2, which impedes the desorption of it and release of NH_3, leading to strong HER competition.[138,139] The doping of Fe was proved to efficaciously modulate the electron density state of the catalyst. The roles of Fe doping for N_2 adsorption, N_2 activation, and NH_3 desorption were further revealed by Sun and coworkers, through a combination of experiments and theoretical calculations.[140] The Fe-doped MoS_2 electrocatalyst demonstrated an NH_3 yield of 20.11 $\mu g\ h^{-1}\ mg_{cat}^{-1}$ at −0.35 V *vs.* RHE, which was significantly higher than that of its MoS_2 and MoS_2–V counterparts. When N_2 molecules were adsorbed on the catalyst, the charge of MoS_2–V was localized between V and N_2 molecules, leading to the strong adsorption ability of N_2, while the electrons of MoS_2–Fe were more concentrated on Mo, which may favor the ammonia release (Fig. 6H–J). According to the free energy profiles, MoS_2–Fe had the lowest rate-determining step (RDS) energy barrier, indicating a more thermodynamically favorable pathway on MoS_2–Fe (Fig. 6K). Their work even provided enlightenment on how to achieve the optimal balance between the three key stages (nitrogen adsorption, hydrogenation, and ammonia desorption) of NRR for superior electrocatalysis by introducing proper doping materials to tune the surface electronic structure.

Progress has also been made in bionic design from FeMoS-nitrogenases.[141] In recent work, Du and coworkers designed a Mo(IV)-doped FeS_2 (FeS_2–Mo) *via* the hydrothermal reaction of $MoCl_5$, $Fe(NO_3)_2$, and thioacetamide.[56] Energy Dispersive Spectrometer (EDS) mapping indicated that Mo, Fe, and S elements were distributed uniformly throughout the nanosheets. Electrochemical measurements suggested that pure FeS_2 presented HER negative and a relatively low yield rate for NH_3. However, the NRR activity was significantly promoted after Mo doping and increased gradually with the Mo content, proving that Mo could act as active sites. The Mo-doped-modified catalyst exhibited a high FE of 14.41% and an NH_3 yield rate of 26.15 $\mu g\ h^{-1}\ mg_{cat}^{-1}$. Afterwards, the optimal pathways for NRR in FeS_2 and FeS_2–Mo were proposed by DFT calculations. Moreover, the doping of Mo opened up an associative distal pathway in FeS_2–Mo, instead of the associative alternating pathway in FeS_2. The reaction energy barrier of the critical dinitrogen hydrogenation step (NN* + H → NNH*) was reduced from 1.24 eV to 0.62 eV. Therefore, the FeS_2 substrate was regarded to suppress the competitive HER, while the doping of Mo favored the adsorption and activation of nitrogen. Similarly, Su *et al.* achieved the suppression of HER by designing atomically dispersed Fe-decorated MoS_2 (Fe–MoS_2).[142] The edge S atoms in MoS_2 were generally considered active sites for HER, while the Mo atoms acted as active centers for NRR.[135] Therefore, better selectivity for NRR could be accomplished by Fe modification of the S sites without shielding the Mo sites to achieve high FE (18.8% at −0.3 V *versus* RHE). DFT calculations proved that the energy barriers of HER in Fe–MoS_2 (0.15 eV) were obviously magnified with respect to pure MoS_2 (0.03 eV). It is worth mentioning that our group predicted and achieved Fe–O–Mo subunits for highly active NRR in Mo-doped Fe_2O_3 (Fig. 7A).[143] The introduction of Mo destroyed the ordered crystal structure and enriched lattice defects, creating more active sites. It also tuned the electronic structures of Fe_2O_3 to enhance the electron injection into N_2, resulting in an elongated and weakened nitrogen bond (Fig. 7C and D). The as-synthesized material showed much higher ammonia yields (21.3 $\mu g\ h^{-1}\ mg_{cat}^{-1}$) and FE (11.2%) than pure Fe_2O_3, proving the significant role of Mo doping (Fig. 7B). An optimized reaction pathway with a lower energy barrier was confirmed on Mo-doped Fe_2O_3(110) in comparison with pristine α-Fe_2O_3(110) (Fig. 7E). Unfortunately, this work could not achieve the doping amount control. It needs further effort to reveal the phase transition mechanism of the catalytic material during the long-term electrocatalytic process.

Doping heteroatoms is effective to promote the electrocatalytic activity of basic materials. Further endeavors should be devoted to disclosing the position of the doping exogenous atom, the coordination and valent state, and the corresponding function during the whole catalytic process.

3.3.1.2. Interface engineering. Interface engineering also provides an effective scheme for conjugate iron and molybdenum compounds. A single material may have too strong or too weak adsorption capacity for nitrogen species, while the hybrid structure can effectively modulate the energy barrier in the reaction stages.[144,145] Abundant active sites and high specific surface area can also be obtained by rational interface engineering.[146,147] Moreover, two or more components could induce electronic coupling and generate a fast electron transport channel to speed up charge transfer.[148–151]

A FeS_2 and MoO_2 nanocomposite anchored on a three-dimensional (3D) graphene aerogel (MoO_2/FeS_2/GA) was developed by Liu and coworkers.[146] FeS_2 and MoO_2 nanoparticles were embedded as active sites to absorb and activate N_2 in an interconnected 3D graphene-based mesoporous aerogel, which provided good conductivity and large accessible specific surface areas. Synergistic effects of such a ternary microstructure exhibited superior electrochemical performance over either single structure, endowed the hybrid catalyst with an impressively high FE of 37.44% and NH_3 yield of 40.18 $\mu g\ h^{-1}\ mg_{cat}^{-1}$ at −0.25 V in 0.1 M HCl. Zhao *et al.* reported Fe nanodot-decorated MoS_2 nanosheets on carbon cloth (Fe–MoS_2/CC) *via* a chemical reduction strategy (Fig. 7F).[152] The strong electronic interaction of Fe and MoS_2 was confirmed by the shift of XPS binding energies of Mo and S and the red shifts in Raman spectra. Furthermore, the effect of Fe loading on the NRR performance was also explored *via* electrochemical measurements. The best NH_3 yield reached 12.5 $\mu g\ h^{-1}\ cm^{-2}$ with a FE of 10.8% at a Fe/MoS_2 mass ratio of 0.077 (Fig. 7G). When the Fe content got too large, the recession in NRR performance was speculated to be attributed to the degraded structures. In another work, FeS-dotted MoS_2 nanosheets covered carbon fiber cloth (CFC) (FeS@MoS_2/CFC) was prepared through a facile

single-step hydrothermal preparation.[54] FeS and MoS_2 uniformly supported the highly conductive CFC and successfully simulated the composition of the active site in FeMoS-cofactor. Notably, it exhibited considerable NRR catalytic activity over a wide pH range.

3.3.1.3. MOF precursors design. Metal–organic frameworks (MOFs) are widely used to design composite electrocatalysts due to their porous structure with high specific surface area for accommodating active sites and facilitating charge/mass transfer.[153–158] Moreover, the desirable nanostructure of the catalysts could be controlled by the morphological structure inheritance of MOFs during thermal annealing processes. The organic ligands in MOFs can be pyrolyzed into porous carbons to improve the conductivity and stability of the derivatives and serve as a support for the active metal sites.[159–162] A handful of excellent reviews have focused on the derived nanomaterials from typical MOFs precursors, including zeolite imidazolate frameworks (ZIFs), Prussian blue analogs (PBAs), as electrocatalysts in energy-related fields, such as hydrogen evolution reaction, oxygen evolution reaction, and oxygen reduction reaction.[157,163–169] These will further provide guidance for advanced materials exploration for NRR electrocatalysis.

Chen *et al.* reported a one-step pyrolysis–phosphating process from MoFe-MOF precursors to fabricate phosphorus-doped carbon microspheres (MoFe-PC), as a cost-effective and highly active catalyst for N_2 fixation under ambient conditions.[170] Electrochemical measurements confirmed that P-doped MoFe-PC (34.23 μg h^{-1} mg_{cat}^{-1}, FE: 16.83%) showed more excellent activity than MoFe–C (24.73 μg h^{-1} mg_{cat}^{-1}, FE: 12.47%). On the one hand, the introduction of P to form a P–C connection increased the conductivity of the hybrids by optimizing the electronic structure. On the other hand, the synergistic interaction between bimetallic oxides and P-doped carbon ensured abundant active sites for the adsorption and activation of nitrogen. Chen and coworkers applied a nanostructure tailoring strategy to successfully synthesize unique hollow Ni_α-$Fe_{1-\alpha}$–MoS_2 nanocubes through vulcanization treatment of Ni–Fe PBA by ammonium thiomolybdate.[171] The as-prepared material showed high stability during the two-hour NRR process at various applied potentials (Fig. 8A). The charge redistribution of the catalyst in an optimal atomic ratio of the NiFe ($\alpha = 0.3$) as compared to the pure MoS_2 was presented by the calculated electron density difference (EDD) mappings (Fig. 8B–C). Based on the electron transfer pathways of Ni_α-$Fe_{1-\alpha}$–MoS_2 catalysts, the spin-polarized density of states, and the corresponding partial density of states, it was suggested that the coupling of S 2p and Mo 3d orbitals generated the $Ni_{0.3}Fe_{0.7}$ active sites, which could easily donate electrons to the absorbed N_2 molecules. Furthermore, a possible pathway of the NRR on the NiFe–MoS_2 NCs catalyst was proposed by electrochemical-FTIR spectroscopy analysis and DFT calculations (Fig. 8D and E). Another Fe-containing MOF precursor, famous as MIL, has also been demonstrated to synthesize Fe_2O_3@MoS_2 composites for NRR electrocatalysis and achieved a remarkable NH_3 yield rate of 112.15 μg h^{-1} mg_{cat}^{-1} and a FE of 8.62%.[150]

Polyoxometalate-based metal–organic frameworks (POMOFs) combine the advantages of both MOFs and POMs to provide specific target structures derived from organic ligands and serve as a source of metals such as Co, Fe, Ni, Mo.[169,172,173] Lately, Ma *et al.* made an exploration using PMo_{12}@MOF-100(Fe)@PVP as a precursor to synthesize $Fe_{1.89}Mo_{4.11}O_7$/FeS_2@C for efficient electrocatalysis of nitrogen reduction (Fig. 8F).[55] Experiments and characterization analysis concluded that the ratio of Fe and Mo could be controlled by accurately regulating the sulfuration time and temperature. Besides, a certain amount of PVP was convinced to be converted into a defected graphitization configuration, according to the intensity ratio of the D band and G band in Raman spectroscopy. Most of the FeS_2 was successfully encapsulated in the graphitic carbon layers leading to obtaining good conductivity. $Fe_{1.89}Mo_{4.11}O_7$/FeS_2@C exhibited an extremely high NH_3 yield of 105.3 μg h^{-1} mg_{cat}^{-1} and a FE of 54.7% at −0.4 V (Fig. 8G), as well as long-period electrolytic stability. The above works open new schemes for the rational design and fabrication of bimetallic MoFe-composites derived from MOFs for NRR. It can be further envisioned that the MOFs and even COFs (COF = covalent organic framework) containing Fe and Mo simultaneously may be used as electrocatalysts and through coordination modulation to regulate the electrocatalytic NRR performance. Moreover, MOFs and COFs may also be utilized as templates or precursors to structurally direct functional nanomaterials with special nano-morphologies, multi-component, and even heterostructures for high-performance NRR electrocatalysis. Thus, Fe,Mo-MOF/COF should be paid much attention to for the materials synthesis and structure design.

3.3.1.4. Ferric molybdate materials. Ferric molybdate materials are a kind of NRR catalysts that are widely available, easy to prepare, and cost-efficient. Wu *et al.* reported a one-step solvothermal method to synthesize $FeMoO_4$ nanorods (NRs) from $FeCl_2$ and Na_2MoO_4.[174] Thanks to synergy interaction between Mo and Fe, the as-prepared $FeMoO_4$ NRs exhibited superior NH_3 yield (17.51 μg h^{-1} mg_{cat}^{-1}) and FE (10.53%) than that of Fe_2O_3 or MoO_3, in 0.1 M Na_2SO_4. The current density remained almost unchanged in the long-term stability test for 12 hours under different applied potentials, indicating superb electrochemical stability. Notably, no N element was included in the raw materials, which helped to prove the source of the product ammonia. The catalytic performance and potential mechanism of $FeMoO_4$ nanorods were also investigated by Chu and workers.[175] The bimetallic nature of $FeMoO_4$ could bring about accelerated electron transport and improved reaction kinetics, and thus it demonstrated a smaller charge transfer resistance than Fe_2O_3 and MoO_3. Besides, the considerable elongation of N–N bond (1.128 Å) and decrease of Mo–N distance (2.014 Å) from Mullikan charge analysis suggested effective $*N_2$ polarization and activation on 3-fold coordinated Mo (Mo_{3c}) (Fig. 9A). Xian *et al.* synthesized $Fe_2(MoO_4)_3$ nanoparticles (FMO-NPs) through a wet chemical process (Fig. 9B).[176] No by-product N_2H_4 was detected during electrolysis, and an impressive NH_3 yield (18.16 μg h^{-1} mg_{cat}^{-1}) and FE (9.1%) were obtained. Ulteriorly, distal and alternating pathways at the $Fe_2(MoO_4)_3$ (110) surface were studied through material calculations (Fig. 9C). The catalyst surface showed strong adsorption of nitrogen molecules, as a deep downhill of −1.22 eV at this step.

Then, the first hydrogenation step ($*N_2 \rightarrow *NNH$) was confirmed to be the PDS. At the following hydrogenation of the N atom, the bond lengths of N≡N and N–Fe showed regular elongation and curtailment, respectively. Importantly, the suitable desorption energy barriers of the distal pathway ensured the smooth release of NH_3 and reaction completion.

The deposition of noble metal nanoparticles is universal to improve the electrocatalytic activity. The above-mentioned iron molybdate materials demonstrate satisfying NRR activities, meanwhile, Au has generally low activity of HER.[177] Therefore, it is a reasonable scheme to introduce Au to optimize the atomic structure of $Fe_2(MoO_4)_3$ and enhance the performances of NRR. Yao *et al.* supported Au on the $Fe_2(MoO_4)_3$ substrate to construct an Au/$Fe_2(MoO_4)_3$ hybrid *via* a facile room-temperature reduction approach, achieving an excellent FE of 18.79% at −0.4 V (Fig. 9E and F).[178] Compared with $Fe_2(MoO_4)_3$ and Au/$Fe_2(MoO_4)_3$ *via* the analysis of temperature-programmed desorption of N_2, the later one showed stronger binding strength of N_2, which originated from the Au regulating promotion. To get a profound understanding of the activation of N≡N, the projected density of states plots of Mo atom and N_2 were calculated. The d-σ and d-π* orbitals hybridization facilitated the electron transfer from Mo 4d orbitals to N_2 2p orbitals (Fig. 9D), thus effectively weakening the inert N≡N triple bond. As a result, the reaction energy barrier of RDS of the distal pathway at Mo active centers was reduced from the former 0.98 to 0.6 eV after Au loading. Unfortunately, these catalytic ferric molybdate materials with large particle sizes suffer from insufficient active sites. In the future, material scientists may develop novel synthetic routes to decrease the size to expose more sites. The electrocatalytic performance can be further enhanced by simultaneous heteroatom doping and heterostructure engineering.

3.3.2 Other Fe-containing bimetallic catalysts. Bimetallic catalysts other than Fe–Mo materials have also been widely studied for heterogeneous surface catalysis due to their flexible compositions.[179] Metal alloys with multiple different active sites have the potential to perform better than pure metals.[180] Consequently, the development of alloy-based heterogeneous electrocatalysts may show NRR activity with several degrees of enhancement compared to pure iron-based electrocatalysts.[181] Xiao *et al.* combined DFT calculations and a computational hydrogen electrode (CHE) model to confirm the efficient catalytic properties of various bimetallic alloys, including CuFe.[182] Das *et al.* systematically modelled iron-rich bimetallic Fe-TM alloy-based structural catalysts by incorporating a first row of TM atoms into the Fe (110) surface. Most Fe-TM alloys were suggested to exhibit reliable stability and Fe–Co material had reasonable *NNH formation with sufficient $*N_2$ activation to be more selective for ammonia production.[183]

Due to the coupling effect, the multicomponent nanostructures generally demonstrate more advanced NRR performance than their individual counterparts.[32,184] Introducing the second metal compound to a Fe-based material will be a compelling strategy to attain further improved performance. For example, doping Co elements into Fe-based materials can be an effective way to rationally regulate the electronic structure of catalysts due to the small atomic size and electronegativity of Co atoms, and the d–d coupling reduces the free energy barrier for N≡N triple bond dissociation. This idea was confirmed experimentally by Chen and coworkers by designing the Co-doped Fe_3S_4 nanoflowers (Fig. 10A). The introduced Co behaved as a new active center to promote N_2 absorption and reduce the energy barrier, achieving a good catalytic performance (Fig. 10B).[185]

Zhang *et al.* prepared heterogeneous Au–Fe_3O_4 nanoparticles (NPs) (Fig. 10C) *via* a one-pot wet-chemical reaction of $HAuCl_4$ and diironnonacarbonyl ($Fe_2(CO)_9$).[184] Such Au–Fe_3O_4 NPs exhibited good performance with a high ammonia yield of 21.42 μg h^{-1} mg_{cat}^{-1} and a favorable FE of 10.54%. The N_2 temperature-programmed desorption (TPD) (Fig. 10D), and surface valence band spectra together confirmed that Au–Fe_3O_4 NPs had a strong synergistic effect for adsorbing reaction species and suitable interface for charge and proton transfer. The theoretical calculations showed that Fe performed as an active site to fix N_2 into $*N_2H$ while the introduction of Au boosted the adsorption of NRR intermediates and provided an energetic-favorable pathway for NRR (Fig. 10E and F). Huang *et al.* developed a Fe_2O_3/Cu composite catalyst by electrodeposition in the presence of $FeCl_2$ and $CuCl_2$ as electrolytes (Fig. 10G), which reached its highest yield of 15.66 μg h^{-1} mg_{cat}^{-1} with a FE of 24.4% at −0.1 V *vs.* RHE.[186] The composite improved the electron transfer on Fe_2O_3, as copper is a good conductor of electrons. As d-band theory suggests, the closer the d-band center approaches the Fermi level, the stronger the adsorption is. The electronic interactions between Fe_2O_3 and Cu elevated the d-state center (Fig. 10H), enabling strong adsorption and back-bonding of N_2 molecules, leading to high catalytic activity.

3.4 Iron boride

Transition metal borides, also known as MBenes, are an emergent class of catalysts that are still in their infancy in the electrochemical NRR field.[187–189] MBenes as NRR electrocatalysts have the advantage of dual active edges from both the exposed metal end and the exposed boride end.[190] In the previous section, we have elaborated on how the electrons and orbitals of iron activate nitrogen bonds. Similarly, boron has three valence electrons in the $2s^2 2p^1$ configuration with an electron-deficient feature and an empty orbital to accept lone pair electrons from N_2. B-to-N π-back bonding could be formed between the sp^3 hybrid orbital of the boron atom and 2p orbital of N_2, which is conducive to N_2 adsorption on the B-active ends (Fig. 11A).[79,191–195]

In a theoretical study, four iron-borides were constructed and explored as potential NRR catalysts, including FeB, FeB_2, $FeB_6(\alpha)$, and $FeB_6(\beta)$ under the framework of DFT (Fig. 11B–E).[58] The authors proposed that Fe–B bonding could remarkably affect Fe–N interaction by examining the free energy differences in reaction pathways on the Fe-sites of FeB_2 and FeB, respectively. Additionally, the NH_3 release issue had been solved by establishing the hypercoordinated $FeB_6(\alpha)$ and $FeB_6(\beta)$. Among these, $FeB_6(\beta)$ offered the lowest ΔG_{max} of 0.68 eV, owing to the

low oxidized Fe in the β-phase. Thus, N_2 could acquire electrons as a newly oxidizing reagent and be activated on the lightly oxidized Fe sites. In the evaluation of selectivity, the calculated ΔG(H*) for the four catalysts is less than the ΔG_{max} of NRR, but H* adsorption is weak in contrast to N_2 adsorption. The heterostructure construction was also applied to design high-performance iron boride-based electrocatalysts. In the current work, the process of NRR was studied on iron atoms supported by B_n-doped graphyne (GY).[196] A distal pathway was successfully identified with a minimum limiting potential of −0.53 V using DFT calculations. Additionally, the FeB@GY surface could effectively promote electron transfer efficiency and significantly improve the stability of intermediate adsorption during NRR. The substitution of B and N atoms for the C atoms in the doped GY structure is suitable for improving surface activity. From the results of the Bader charge analysis and charge density difference, it was detected that the reaction intermediates could not only accept electrons but also extract electrons from FeB@GY. The analysis of the partial density of states indicated a strong interaction between Fe-3d and N-2p in addition to B-2p, which was caused by the existence of the overlapped orbitals.

Chu's group pioneered the experimental synthesis of amorphous FeB_2 porous nanosheets (α-FeB_2 PNSs) through a facile reflux method.[57] Amorphization engineering produced vast unsaturated coordination sites and surface-exposed defects, which served as active sites to promote the electrocatalytic reaction energetics and kinetics. In 0.5 M $LiClO_4$ electrolyte, α-FeB_2 PNSs showed a maximum NH_3 yield rate of 39.8 μg h^{-1} mg_{cat}^{-1} at −0.3 V and a FE of 16.7% at −0.2 V. Furthermore, the chrono-potentiometric response showed no obvious decays for 20 h of consecutive electrolysis, with a 92.8% retention of the initial NH_3 yield, indicating excellent long-term stability. In this work, crystalline FeB_2 PNSs (c-FeB_2 PNSs) were also prepared by annealing at 600 °C for 3 h (Fig. 11F). When comparing the NRR performance, c-FeB_2 showed smaller ECSA and weaker N_2 absorption than a-FeB_2. Meanwhile, a-FeB_2 had strong charge transfer between $*N_2$ and active substrates and more injected electrons to activate the N_2 molecule to a greater extent, as observed in Fig. 11G. A lower G_{*N_2H} (0.45 eV) on a-FeB_2 was provided to stabilize $*N_2H$ and reduce the initial reduction barrier (Fig. 11H). Currently, most research on TMBs (TM = transition metal) especially iron borides as NRR electrocatalysts is focused on the theoretical calculations.[58,197–200] There is a deficiency of reports about experimental fruits on iron borides for NRR electrocatalysis, probably due to the harsh preparation conditions.

3.5 Fe-based single-atom catalysts

Up to now, single-atom catalysts (SACs), for which isolated atoms are anchored on various substrates to generate stable configuration, have been extensively investigated for nitrogen reduction reactions.[34,201–204] Compared with traditional catalyst materials, decreasing metal nanoparticles into single atoms can significantly improve the catalytic activity and selectivity towards NRR.[205] The SACs may maximize atom utilization and effectively reduce economic costs in large-scale industrial production.[206–208] Meanwhile, the high dispersibility of SACs ensures their larger specific surface area and more exposed active sites, leading to stronger catalytic activity.[202,209] Moreover, the selection of substrate plays an important role in improving anchoring stability and modulating the electronic structure of SACs.[207,210] The interactions between substrates and loaded metal atoms give rise to tunable electronic structures, which favors the adsorption and activation pathway of the reactants at the catalytic sites to lower the energy barrier of NRR, in conjunction with unsaturated coordination environments.[211,212] However, some problems still exist when single atoms are applied as catalysts such as low stabilities for long cycle catalysis, low active metal atom loadings, difficulties in efficiently dispersing and isolating individual atoms, and the complex preparation process.[213,214] As a result, developing suitable substrates to achieve stable and efficient loading of single atoms is an urgent need.

Nitrogen-doped carbon is one of the most encouraging candidates due to its enhanced electronic conduction, optimized charge distribution, and electronic structure of active sites, which is caused by the interfacial interactions between iron atoms and the surrounding nitrogen/carbon atoms.[210] As revealed by DFT calculations, atomically dispersed Fe–N_3 site on nitrogen-doped graphene (Fe–N_3/graphene) can substantially activate the inert N≡N bond of N_2 with high spin-polarization and a localized magnetic moment.[215] Yang *et al.* anchored Fe single-atoms on a nitrogen-doped carbon substrate (Fe SAC/N–C) to realize the coordination structure of Fe–N_3.[210] The HAADF-STEM images indicated that the majority of Fe objects were downsizing to single atoms with a range of 0.1 to 0.2 nm, and there were no obvious Fe nanoparticles or clusters. The catalyst achieved an enhanced NH_3 yield rate of 53.12 μg h^{-1} mg_{cat}^{-1} and a high FE of 39.6% in 0.1 M KOH with ignored decay in seven consecutive electrolysis cycles. Computational studies provided direct evidence of the robust binding capability of Fe–N_3 catalytic active sites to N_2 molecules to achieve the high selectivity of Fe SAC/N–C for NH_3 formation. The calculated Gibbs free energy diagrams illustrated that the alternating pathway was a more convincing mechanism on highly dispersed Fe sites compared with the distal pathway, as its lower energy barrier of ΔG = 0.915 eV (Fig. 12A).

Fe–N_4 configurations are also developed for electrocatalytic ammonia synthesis. He *et al.* reported an atomically dispersed iron phthalocyanine (FePc) molecules on porous carbon with Fe–N_4 coordination structure, which achieved a dramatically high NH_3 yield rate of 137.95 μg h^{-1} mg_{cat}^{-1} at a low potential of −0.3 V (*vs.* RHE).[216] The SEM image showed the comb-like structure of 3D carbon substrate with massive nanopores, which contributed to the high loading ability of 7.43 wt% (the loading of FePc) (Fig. 12B). The current density decreased significantly in poisoning treatment by SCN^- suggests that the Fe center of FePc is the dominant active site for NH_3 formation. Liu *et al.* explored the realization of high Fe–N_4 loading capacity.[213] Fe-TPP, $C_5H_8N_2$, and *N*,*N*-diethylformylamide (DEF) *etc.* were milled in a zirconia-ball grinding mill to form the Fe-TPP⊂rho-ZIF precursor, and Fe–N/C was obtained by pyrolyzing in a tube heating furnace at 950 °C for 3 h under an N_2

atmosphere (Fig. 12C). The HAADF-STEM image indicated that the Fe atoms were uniformly distributed on the carbon substrate, in which the Fe single-atom loading reached 3.5 wt% (Fig. 12D). The sublimation of Zn in the pyrolysis process of the precursor was favorable to expose the catalytic sites and increase the specific surface area,[217] which reached up to 1088.96 $m^2 g^{-1}$. Wang *et al.* reported a Fe_{SA}–N–C catalyst with an extremely high FE of over 56.55% (Fig. 12E).[218] Single Fe atoms were uniformly loaded throughout the N-doped carbon support, and no Fe nanoparticles or aggregations were obviously detected. The adsorption behavior of N_2 toward Fe active sites was illustrated by molecular dynamics simulations, which suggested a lower energy barrier of 2.38 kJ mol^{-1} at approximately 0.54 nm for efficient N_2 access. As depicted in Fig. 12F, the alternating pathway with lower energy uphill of 0.28 eV was more favorable than the distal pathway. Additionally, the high energy barriers (2.91 eV) for *H adsorption resulted, in particular, sluggish HER kinetics. Based on the above characteristics, the desired selectivity and FE were achieved by enhancing nitrogen reduction and suppressing hydrogen evolution.

Fe SACs that anchored on strain-engineered graphene substrates were modeled and systematically examined by first-principles calculations, suggesting that curvature strongly influences the catalytic activity and selectivity of SACs for NRR.[219] Bu *et al.* studied the NRR pathways for a dual-atom Fe_2 species on graphitic carbon nitride (g-C_3N_4) by changing external conditions.[220] It was found that applying an appropriate range of tensile to the graphitic carbon nitride (g-C_3N_4) substrate could reduce the overpotential values, which arose from a break in the intrinsic scaling relationship of the adsorption energy between the *N_2 and *HNN adsorbates. More influences of structural distortion on the NRR catalytic properties of Fe, N codoped carbon (Fe–N–C) were explored.[221] The NRR intermediate species *NNH could be strongly bound at the FeN_4 and FeN_3 active sites embedded in strained graphene layers, contributing to the enhanced NRR activity. In contrast to *NNH, *H showed a greater adsorption energy barrier, which indicated the less favored competitive HER and higher selectivity of NRR. Their computational work provides evidence for improving the catalytic activity and selectivity of Fe–N–C materials towards NRR by tuning the degree of compressive strain in their graphene layers. Although the theoretical studies of strain engineering on Fe-SACs have achieved promising results, the predictions need to be further confirmed by experimental works.

The doping of multi-element atoms into the substrate is an effective and well-explored strategy for adjusting the Fe active site configuration to enhance NRR. Wang *et al.* developed boron-induced electron-rich SACs (Fe–B/NC) by dispersing single Fe sites on boron, nitrogen-co-doped carbon.[222] The desired selectivity and stability were proved by no detectable N_2H_4 and six recycling tests (Fig. 12G). The introduction of B atoms with low electronegativity ($\chi = 2.0$) broke the symmetric electron distribution of the Fe–N_4 coordination, engendering electron donor (B)/acceptor (N) pairs along the B–Fe–N bridge to enhance electron transfer. After being adsorbed on B–Fe sites, the triple bond in N_2 was elongated by 0.115 Å with a comparison of free N_2, due to back-donation from B and Fe to N_2, which was confirmed by the Bader charge after N_2 adsorption analysis (Fig. 12H). Moreover, the coupling with B 2p could delocalize the electrons in the Fe 3d orbital (Fig. 12I), increasing the electron conductivity for N_2 adsorption/activation, thereby enhancing the NRR performance. In addition, the catalyst exhibited a hindered effect on HER relative to the boron-free sample, owing to a large ΔG_{H^*} (Fig. 12J). Another coordination mode for anchoring Fe SA has also been explored, typically as Fe-$(O–C_2)_4$ single-atom sites on lignocellulose-derived carbon with impressive catalytic activity (32.1 μg h^{-1} mg_{cat}^{-1} equal to 5350 μg h^{-1} mg_{Fe}^{-1}), by Zhao and coworkers.[45]

In addition to nitrogen-doped carbon, other substrates also can be applied to support Fe single atoms as SACs for NRR. Porous materials with large surface areas or vacancies are ideal supports that can accommodate ample active sites, realizing the high metal loading. Chen *et al.* prepared S-coordinated Fe SACs on mesoporous TiO_2 (Fe_1S_x@TiO_2), which were constructed by a lattice-confined strategy.[60] FeS_2O_2 sites were confirmed as active centers by theoretical calculations. No peak was observed for a Fe–Fe bond in the Fe-K edge EXAFS spectra of Fe_1S_x@TiO_2, indicating that Fe atoms are distributed individually (Fig. 13A). Abundant OVs and Ti–S coordination bonds were detected by Ti K-edge EXAFS spectra, resulting in high dispersion stability. The finite element analysis showed that confinement of opened and ordered mesopores could promote mass transfer and provide a large active surface area. As a result, the catalyst showed a good NH_3 production rate of 18.3 μg h^{-1} mg_{cat}^{-1} with 17.3% FE, and the origin of NH_3 was verified *via* an isotopic-labeling experiment (Fig. 13B). Moreover, the relationship between Fe loading capability and NRR performance was also investigated, when the ratio of Fe : Ti is 6 : 100, NRR activity reached maximum without Fe aggregation. First-principles calculations revealed the existence of an enzymatic mechanism with a low overpotential of 0.21 V and side-on adsorption of N_2 in MoS_2-supported Fe_2 clusters (Fe_2/MoS_2), which is conducive to effective N≡N bond activation.[223] Li *et al.* creatively designed a single Fe atom supported on atomically thin molybdenum disulfide (SACs-MoS_2–Fe) to form high curvatures with interfacial protrusion-like shape (Fig. 13C).[224] Triggering interfacial polarization by curvature-rich surface and interface demonstrates potential universality in wide-scope electrocatalysis, including the promising and energy-effective breaking of N≡N bond. Fe single atoms worked as external adatoms conjugating with MoS_2 to create 3D protrusions, instead of interior dopants substituting in MoS_2 skeletons, which was distinct from extensively reported metal–N_x and defect-trapped-SACs. The unique geometry stimulated electron injection into N≡N efficiently enabled N_2 polarization and reduction. When the atomic ratio of Fe and MoS_2 reached 2.0, SACs-MoS_2–Fe_2 demonstrated the best catalytic performance of ammonia yield (97.5–6 μg h^{-1} cm^{-2}) and FE (31.6–2%) at −0.2 V.

Diatomic catalysts (DACs) derived from single-atom catalysts have been widely explored for highly efficient electrocatalysis.[225–228] According to related investigations, the catalytic activity of graphene-based Mn, Ni, Co, and Fe DACs exceeds that of the corresponding SACs.[229,230] Zhang and

coworkers reported FeMo/NC DSACs as a "dual-site" material by anchoring isolated Fe and Mo atoms on hierarchical N-doped carbon nanotubes.[231] This catalyst demonstrated an NH_3 yield of 26.8 μg h^{-1} mg_{cat}^{-1} and a FE of 11.8, which is 1.6 and 2.5 times larger than those of Mo/NC and Fe/NC. Time-dependent *in situ* Fourier transform infrared spectroscopy (*in situ* FTIR) measurements were conducted for dual-site FeMo/NC DSACs and single-site Fe/NC and Mo/NC to investigate the synergy mechanism of Mo and Fe single atoms (Fig. 13D). Three positive-going bands of N–N stretching, $–NH_2$ wagging, and H–N–H bending were appeared at the *in situ* FTIR spectra of FeMo/NC, suggesting the formation of $*N_2H_y$ intermediates during the NRR process. No positive-going N═N stretching was observed on the FeMo/NC surface, which implied that the $*N_2H_x$ intermediates ($0 \leq x \leq 2$) had no obstacle to separate into a single bond N–N of $*N_2H_y$ intermediates ($1 \leq y \leq 4$). The NRR over FeMo/NC may follow an associative mechanism (Fig. 13E), due to the existence of the three main intermediates, as well as no N_2H_4 was detected. Ma *et al.* revealed the catalytic principle of Fe/Mo–N–C from the point of view of the spin moment of the active centers through theoretical calculations.[232] The neighboring Fe could modulate the spin state of the Mo center in MoN_4 to switch from a high-spin state to a medium-spin state, effectively relieving the strong overlap between the Mo 4d orbital and the N_xH_y intermediates, facilitating the desorption of NH_3, and ultimately leading to a lower overpotential. Recent work reported that an extraordinary NRR performance of 579.2 ± 27.8 μg h^{-1} mg_{cat}^{-1} NH_3 yield rate and 79.0 ± 3.8% FE could be achieved on an atomically dispersed, bimetallic Fe–Co active site catalyst (Fe/Co–O–C-*r*) (Fig. 13F).[233] The observation and fitting of EXAFS spectra of Fe/Co–O–C-1.0 suggested that the atomically dispersed Fe, Co atoms are anchored on carbonized BC (CBC) by a bimetallic Fe–Co arrangement anchoring to graphitic carbon through six O-bridging bonds, for which, $[(O–C_2)_3Fe–Co(O–C_2)_3]$ is the likely bimetallic unit (Fig. 13G). Calculations pointed out that an energy-favorable transformation from $[(O–C_2)_3Fe–Co(O–C_2)_3]$ to $[(O–C_2)_3Fe–Co(O–C)C_2]$ can occur at the end of an NRR cycle on desorption of $*NH_3$. $[(O–C_2)_3Fe–Co(O–C)C_2]$ was further confirmed to be the actual active site of Fe/Co–O–C-*r* and resulted in remarkable NRR performance.

Traditional SACs have the inherent disadvantage that single metal atoms tend to agglomerate due to their large surface free energy. Avoiding the aggregation of individual atoms at the expense of low metal loading limits the improvement of NRR performance and practical applications. A new variety of SACs, single-atom alloys (SAAs), in which, the isolated metal atoms are anchored on the substrate metal has been proposed with integrated merits.[234–236] Specifically, the extremely strong metal–support interactions endow the high thermodynamic stability to break limitations in metal loading. Moreover, the alloying effect of SAAs tunes the electronic structure of atomic metal sites to enable an advantageous balance between the appropriate binding of intermediates and the effective dissociation of reactants. Li *et al.* first developed a $PdFe_1$ single-atom alloy metallene, which demonstrated an NH_3 yield of 111.9 μg h^{-1} mg_{cat}^{-1} and a FE of 37.8% at −0.2 V *vs.* RHE.[59] Preliminary theoretical computations indicated the enhancement of N_2 affinity on $PdFe_1$ and the Lewis acid–base interaction facilitated the following N_2 polarization and cleavage (Fig. 13H). In the free energy diagrams, the energy barrier of the rate-limiting step was reduced to 0.72 eV, due to the efficient N_2 activation on Fe sites. Encouraged by the above theoretical results, the preconceived $PdFe_1$ (Fe: 3.91 at%) was prepared *via* a one-step wet chemistry strategy. The low-peak-intensity spots in 3D topographic atom images suggested that Fe atoms successfully substituted the partial Pd atoms on the $PdFe_1$ substrate (Fig. 13I). Thus, this stably distributed the SAA catalyst and presented a steady current density during the 100 h of continuous electrolysis in chronoamperometry, and no apparent recession in NRR yields and FEs within ten cycling tests were observed.

4. Conclusions and outlook

Significant and encouraging advancements in ambient electrochemical NRR for gaseous nitrogen molecules to NH_3 have been made in the past five years and even the decade. However, efficient nitrogen reduction under ambient conditions faces challenges for both fundamental research and practical applications. These substantial barriers include, for example, the inertness and low water solubility of N_2 molecules, weak N_2 adsorption on catalyst surfaces, high overpotentials, low catalytic lifetimes, and the involvement of multi-proton and multi-electron pathways leading to low selectivity. To negotiate these obstacles and achieve efficient NRR with a high production rate, high FE, and high energy utilization efficiency, functional Fe-based materials have been paid much attention to and explored for this promising field, possibly inspired by both the Fe-containing industrial catalyst and biological enzyme. In this review, a brief catalytic mechanism for the electrocatalytic NRR and a comprehensive overview of the research fruits of Fe-based electrocatalytic materials for NRR are presented. Table 1 summarized and compared the electrocatalytic performances of the representative Fe-based electrocatalysts, including iron oxide, sulfides, bimetallic Fe-containing materials, single-atom, and even dual-atomic materials. Unfortunately, the activity, selectivity, and longevity of the Fe-based materials and others are not satisfactory. Therefore, to optimize the electrocatalytic performance and further promote significant development, we propose the following perspectives and further development directions (Fig. 14).

4.1 From an in-depth mechanistic reaction pathway

According to the possible associative distal/alternating pathway, and enzymatic pathway, the nitrogen adsorption ability, activation ability, and even the N_2 adsorption mode of the metal site are very crucial. The Fe element with variable valence will be endowed with different electronic configurations.[238] Furthermore, the crystal field and the local coordination environments can be further elaborately designed to modulate the spin states, including high spin, low spin, and even intermedia spin, of the Fe center.[71] It may provide a perspective solution to strengthen the activation ability. From another point of view, the

microscopic reaction mechanism indicates that the hydrogenation process is another key factor to complete NRR. However, few researchers pay attention to hydrogen sources, especially for the hydrogen intermediate H* in the pathway and their transfer process. Wang and coworkers recognized that the directly significant suppression of HER may be counterproductive for electrocatalytic NRR because N_2 hydrogenation also needs active H species.[239] It is anticipated that scientific research should focus more on the solution of the intermedia H*-related issues, including its source, its production, its transfer, and subsequent hydrogenation for N_2. Understanding these above two key points may provide meaningful guidance to explore catalytic materials with advanced structures and performances.

4.2 Exploring coupling strategies for materials design

The strategies of enzyme mimicking, elemental doping, heterostructures engineering, and single-atom dispersion on functional supports, *etc.* presented in this review have all yielded exciting results. These tactics are usually adopted to optimize the binding energy of the reactants and key intermediates through the synergistic effect, thereby enhancing the intrinsic per-site activity. More exposed active sites will promote the electrochemical reaction, which is believed to maximize extrinsic activity. Advanced nanoarchitectures, such as 2D nanosheets, hierarchical structures, and porous structures are advantageous to facilitate charge/mass transportation. Moreover, the compositions and the local coordination environments are also needed to disclose their importance. These mentioned strategies are not single-functioned and not self-governed. A deeper understanding and sensible coupling of these strategies can further improve both the intrinsic and extrinsic catalytic activity of iron-based catalysts, simultaneously.[240] According to the first point of perspective, the creation of multi-model active sites may be efficient to improve the catalytic performance. The real function of each site and their distance, interaction, or synergistic effect should be further investigated in depth. Therefore, it is of great significance to develop new synthetic methods to accomplish the above coupling strategies and analyze the design principles that would provide great opportunities for rational exploration of superior NRR electrocatalysts.

4.3 Establishing viable and standard protocols for electrocatalytic NRR evaluation

Up to now, the researchers have used different methods to quantify produced ammonia, including commonly used colorimetry (indophenol blue and Nessler's reagent), ion chromatography, and NMR.[241] Unfortunately, some of them are not completely reliable. For example, ion chromatography detection is susceptible to interference from other cations (*e.g.* Li^+, K^+, *etc.*). Therefore, it is recommended to integrate multiple methods under repeatable experiments to produce meaningful data with an error bar. In order to exclude exogenous nitrogen pollutants (NH_3, nitrate/nitrite, and nitrous oxide), the N_2 feed gas, electrolytes, and electrocatalysts need to be purified for NRR tests. It is necessary to conduct isotope ($^{15}N_2$) labelling experiments to identify the origin of the ammonia, a key experiment to verify the true electrocatalytic positive. Moreover, the configurations of the electrolytic cell may be further studied to guide its rational design. The flow cell within an enclosed system may be better to ensure a continuous supply of nitrogen with enough solubility to the catalyst surface. It will also realize the cycling of $^{15}N_2$ to reduce both economic cost and contamination. It is also urgently required to develop more selective, precise, real-time on-line methods for NH_3 determination. Therefore, it is a burdensome system engineering to standardize the evaluation protocol, yet, is of great significance for materials comparison, and this NRR field is rapidly growing.

4.4 Combining theoretical calculations and *in situ* characterizations

The true reaction pathway in electrocatalytic NRR is expected to unravel from fundamental research that integrates experiments and theoretical calculations. *In situ*/*operando* measurements by various techniques, such as surface-enhanced infrared absorption spectroscopy, Raman, near ambient-pressure X-ray photoelectron spectroscopy (NAP-XPS), X-ray absorption spectroscopy (XAS) by synchrotron radiation and others, can directly define $*N_xH_y$ intermediate products, revealing the actual catalytic active sites and even understand the deactivation reasons.[242] These will help researchers to clarify the elementary reactions during the NRR process and build up more valid structure models for theoretical investigations. Great endeavors will be devoted to investigating the adsorption strength of different intermediates, and the Gibbs free energy change during NRR, helping to reveal the mechanism from a theoretical view. Improving the resolution of these operando techniques and providing a programmable measurement database are needed. Different *in situ* methods with varying functions are recommended for in-depth investigations. The combination of theoretical calculations and *in situ* characterizations would bridge the gap between mechanistic thoughts and experimental electrocatalytic performances.[243] It will further underpin the structure–property relationships and guide new directions for electrocatalytic materials design.

Conflicts of interest

There are no conflicts to declare.

Acknowledgements

The authors are grateful for the financial support from the National Natural Science Foundation of China (No. 22271036), the Fundamental Research Funds for the Central Universities of China (DUT22LK15), and the Open Funds of the State Key Laboratory of Rare Earth Resource Utilization (RERU2022011).

Notes and references

1 J. Deng, J. A. Iñiguez and C. Liu, *Joule*, 2018, **2**, 846–856.

2 S. Chen, X. Liu, J. Xiong, L. Mi, X.-Z. Song and Y. Li, *J. Mater. Chem. A*, 2022, **10**, 6927–6949.
3 A. Liu, Y. Yang, X. Ren, Q. Zhao, M. Gao, W. Guan, F. Meng, L. Gao, Q. Yang, X. Liang and T. Ma, *ChemSusChem*, 2020, **13**, 3766–3788.
4 H. Shen, C. Choi, J. Masa, X. Li, J. Qiu, Y. Jung and Z. Sun, *Chem*, 2021, **7**, 1708–1754.
5 F. Rehman, M. Delowar Hossain, A. Tyagi, D. Lu, B. Yuan and Z. Luo, *Mater. TodayMater. Today*, 2021, **44**, 136–167.
6 M. Arif, M. Babar, U. Azhar, M. Sagir, M. Bilal Tahir, M. Asim Mushtaq, G. Yasin, M. Mubashir, J. Wei Roy Chong, K. Shiong Khoo and P. Loke Show, *Chem. Eng. J.*, 2023, **451**, 138320.
7 W. Guo, K. Zhang, Z. Liang, R. Zou and Q. Xu, *Chem. Soc. Rev.*, 2019, **48**, 5658–5716.
8 Q. Wang, J. Guo and P. Chen, *J. Energy Chem.*, 2019, **36**, 25–36.
9 K. Ithisuphalap, H. Zhang, L. Guo, Q. Yang, H. Yang and G. Wu, *Small Methods*, 2018, **3**, 1800352.
10 T. Wu, W. Fan, Y. Zhang and F. Zhang, *Mater. Today Phys.*, 2021, **16**, 100310.
11 R. Zhao, H. Xie, L. Chang, X. Zhang, X. Zhu, X. Tong, T. Wang, Y. Luo, P. Wei, Z. Wang and X. Sun, *EnergyChem*, 2019, **1**, 100011.
12 L. Niu, L. An, X. Wang and Z. Sun, *J. Energy Chem.*, 2021, **61**, 304–318.
13 S. Zhang, Y. Zhao, R. Shi, G. I. N. Waterhouse and T. Zhang, *EnergyChem*, 2019, **1**, 100013.
14 V. Rosca, M. Duca, M. T. de Groot and M. T. Koper, *Chem. Rev.*, 2009, **109**, 2209–2244.
15 C. Zhang, Z. Wang, J. Lei, L. Ma, B. I. Yakobson and J. M. Tour, *Small*, 2022, **18**, e2106327.
16 G. Soloveichik, *Nat. Catal.*, 2019, **2**, 377–380.
17 L. Du, L. Xing, G. Zhang, X. Liu, D. Rawach and S. Sun, *SusMat*, 2021, **1**, 150–173.
18 Y. Yao, J. Wang, U. B. Shahid, M. Gu, H. Wang, H. Li and M. Shao, *Electrochem. Energy Rev.*, 2020, **3**, 239–270.
19 X. Zhu, S. Mou, Q. Peng, Q. Liu, Y. Luo, G. Chen, S. Gao and X. Sun, *J. Mater. Chem. A*, 2020, **8**, 1545–1556.
20 X. W. Lv, C. C. Weng and Z. Y. Yuan, *ChemSusChem*, 2020, **13**, 3061–3078.
21 B. Ma, H. Zhao, T. Li, Q. Liu, Y. Luo, C. Li, S. Lu, A. M. Asiri, D. Ma and X. Sun, *Nano Res.*, 2020, **14**, 555–569.
22 Y. Pang, C. Su, G. Jia, L. Xu and Z. Shao, *Chem. Soc. Rev.*, 2021, **50**, 12744–12787.
23 Y. Fu, T. Li, G. Zhou, J. Guo, Y. Ao, Y. Hu, J. Shen, L. Liu and X. Wu, *Nano Lett.*, 2020, **20**, 4960–4967.
24 X. Guo, X. Wan and J. Shui, *Cell Rep. Phys. Sci.Cell Rep. Phy. Sci.*, 2021, **2**, 100447.
25 L. Zhang, X. Xue, M. Gao, J. Zhao, T. Yan, C. Yu, L. Zhao, X. Ren and Q. Wei, *New J. Chem.*, 2021, **45**, 11457–11460.
26 W. Zhang, K. Mao, J. Low, H. Liu, Y. Bo, J. Ma, Q. Liu, Y. Jiang, J. Yang, Y. Pan, Z. Qi, R. Long, L. Song and Y. Xiong, *Nano Res.*, 2021, **14**, 3234–3239.
27 Y. Zhang, J. Hu, C. Zhang, Q. Qi, S. Luo, K. Chen, L. Liu and M. K. H. Leung, *J. Mater. Chem. A*, 2021, **9**, 5060–5066.
28 H. Wang, J. Si, T. Zhang, Y. Li, B. Yang, Z. Li, J. Chen, Z. Wen, C. Yuan, L. Lei and Y. Hou, *Appl. Catal., B*, 2020, **270**, 118892.
29 R. Zhao, C. Liu, X. Zhang, X. Zhu, P. Wei, L. Ji, Y. Guo, S. Gao, Y. Luo, Z. Wang and X. Sun, *J. Mater. Chem. A*, 2020, **8**, 77–81.
30 G. Deng, T. Wang, A. A. Alshehri, K. A. Alzahrani, Y. Wang, H. Ye, Y. Luo and X. Sun, *J. Mater. Chem. A*, 2019, **7**, 21674–21677.
31 H.-M. Liu, S.-H. Han, Y. Zhao, Y.-Y. Zhu, X.-L. Tian, J.-H. Zeng, J.-X. Jiang, B. Y. Xia and Y. Chen, *J. Mater. Chem. A*, 2018, **6**, 3211–3217.
32 H. Bai, F. Wang, Y. Liu, C. Ma, J. Ding and W. Fan, *Colloids Surf., A*, 2022, **655**, 130312.
33 C. Lv, C. Yan, G. Chen, Y. Ding, J. Sun, Y. Zhou and G. Yu, *Angew. Chem., Int. Ed.*, 2018, **130**, 6181–6184.
34 L. Han, X. Liu, J. Chen, R. Lin, H. Liu, F. Lu, S. Bak, Z. Liang, S. Zhao, E. Stavitski, J. Luo, R. R. Adzic and H. L. Xin, *Angew. Chem., Int. Ed.*, 2019, **58**, 2321–2325.
35 X. Zhao, G. Hu, G. F. Chen, H. Zhang, S. Zhang and H. Wang, *Adv. Mater.*, 2021, **33**, e2007650.
36 Z. Wang, F. Gong, L. Zhang, R. Wang, L. Ji, Q. Liu, Y. Luo, H. Guo, Y. Li, P. Gao, X. Shi, B. Li, B. Tang and X. Sun, *Adv. Sci.*, 2019, **6**, 1801182.
37 P. Wei, H. Xie, X. Zhu, R. Zhao, L. Ji, X. Tong, Y. Luo, G. Cui, Z. Wang and X. Sun, *ACS Sustainable Chem. Eng.*, 2019, **8**, 29–33.
38 P. Zhao, Z. Lu and S. Liu, *J. Nanosci. Nanotechnol.*, 2018, **18**, 3348–3355.
39 C. Ling, Y. Ouyang, Q. Li, X. Bai, X. Mao, A. Du and J. Wang, *Small Methods*, 2018, **3**, 1800376.
40 C. N. R. Rao and G. Ranga Rao, *Surf. Sci. Rep.*, 1991, **13**, 223–263.
41 Y. Li, Y. Ji, Y. Zhao, J. Chen, S. Zheng, X. Sang, B. Yang, Z. Li, L. Lei, Z. Wen, X. Feng and Y. Hou, *Adv. Mater.*, 2022, **34**, e2202240.
42 D. Zheng, N. Wang, M. Wang, S. Ding, C. Ma, M. Y. Darensbourg, M. B. Hall and L. Sun, *J. Am. Chem. Soc.*, 2014, **136**, 16817–16823.
43 J. Luo, Y. Hu, L. Xiao, G. Zhang, H. Guo, G. Hao and W. Jiang, *Nanotechnology*, 2019, **31**, 085708.
44 X. Cui, C. Tang, X. M. Liu, C. Wang, W. Ma and Q. Zhang, *Chem.–Eur. J.*, 2018, **24**, 18494–18501.
45 S. Zhang, M. Jin, T. Shi, M. Han, Q. Sun, Y. Lin, Z. Ding, L. R. Zheng, G. Wang, Y. Zhang, H. Zhang and H. Zhao, *Angew. Chem., Int. Ed.*, 2020, **59**, 13423–13429.
46 M. Yang, Z. Jin, C. Wang, X. Cao, X. Wang, H. Ma, H. Pang, L. Tan and G. Yang, *ACS Appl. Mater. Interfaces*, 2021, **13**, 55040–55050.
47 Q. Li, Y. Guo, Y. Tian, W. Liu and K. Chu, *J. Mater. Chem. A*, 2020, **8**, 16195–16202.
48 W. Tong, B. Huang, P. Wang, Q. Shao and X. Huang, *Natl. Sci. Rev.*, 2021, **8**, nwaa088.
49 H. Ying, T. Chen, C. Zhang, J. Bi, Z. Li and J. Hao, *J. Colloid Interface Sci.*, 2021, **602**, 64–72.

50 H. Q. Xie, X. Zheng, Q. Y. Feng, X. P. Chen, Z. H. Zou, Q. X. Wang, J. Tang, Y. Li and Y. Ling, *ChemSusChem*, 2022, **15**, e202200919.
51 X. Wang, J. Zheng, P. Li, X. B. Yin, S. Wang, B. Zhang, J. Xu and M. Zhang, *Dalton Trans.*, 2022, **51**, 3170–3179.
52 H. Wang, Z. Li, Y. Li, B. Yang, J. Chen, L. Lei, S. Wang and Y. Hou, *Nano Energy*, 2021, **81**, 105613.
53 Y. Zhao, F. Li, W. Li, Y. Li, C. Liu, Z. Zhao, Y. Shan, Y. Ji and L. Sun, *Angew. Chem., Int. Ed.*, 2021, **60**, 20331–20341.
54 Y. Guo, Z. Yao, B. J. J. Timmer, X. Sheng, L. Fan, Y. Li, F. Zhang and L. Sun, *Nano Energy*, 2019, **62**, 282–288.
55 X. Wang, Z. Feng, B. Xiao, J. Zhao, H. Ma, Y. Tian, H. Pang and L. Tan, *Green Chem.*, 2020, **22**, 6157–6169.
56 H.-B. Wang, J.-Q. Wang, R. Zhang, C.-Q. Cheng, K.-W. Qiu, Y.-j. Yang, J. Mao, H. Liu, M. Du, C.-K. Dong and X.-W. Du, *ACS Catal.*, 2020, **10**, 4914–4921.
57 K. Chu, W. Gu, Q. Li, Y. Liu, Y. Tian and W. Liu, *J. Energy Chem.*, 2021, **53**, 82–89.
58 Q. Li, C. Liu, S. Qiu, F. Zhou, L. He, X. Zhang and C. Sun, *J. Mater. Chem. A*, 2019, **7**, 21507–21513.
59 X. Li, P. Shen, Y. Luo, Y. Li, Y. Guo, H. Zhang and K. Chu, *Angew. Chem., Int. Ed.*, 2022, **61**, e202205923.
60 J. Chen, Y. Kang, W. Zhang, Z. Zhang, Y. Chen, Y. Yang, L. Duan, Y. Li and W. Li, *Angew. Chem., Int. Ed.*, 2022, **61**, e202203022.
61 L. Zhang, G. F. Chen, L. X. Ding and H. Wang, *Chem.–Eur. J.*, 2019, **25**, 12464–12485.
62 K. C. Macleod and P. L. Holland, *Nat. Chem.*, 2013, **5**, 559–565.
63 C. J. van der Ham, M. T. Koper and D. G. Hetterscheid, *Chem. Soc. Rev.*, 2014, **43**, 5183–5191.
64 H. P. Jia and E. A. Quadrelli, *Chem. Soc. Rev.*, 2014, **43**, 547–564.
65 K. Honkala, A. Hellman, I. N. Remediakis, A. Logadottir, A. Carlsson, S. Dahl, C. H. Christensen and J. K. Norskov, *Science*, 2005, **307**, 555–558.
66 S. Wang, F. Ichihara, H. Pang, H. Chen and J. Ye, *Adv. Funct. Mater.*, 2018, **28**, 1803309.
67 X. L. Ma, J. C. Liu, H. Xiao and J. Li, *J. Am. Chem. Soc.*, 2018, **140**, 46–49.
68 X. Cui, C. Tang and Q. Zhang, *Adv. Energy Mater.*, 2018, **8**, 1800369.
69 J. G. Howalt, T. Bligaard, J. Rossmeisl and T. Vegge, *Phys. Chem. Chem. Phys.*, 2013, **15**, 7785–7795.
70 E. Skulason, T. Bligaard, S. Gudmundsdottir, F. Studt, J. Rossmeisl, F. Abild-Pedersen, T. Vegge, H. Jonsson and J. K. Norskov, *Phys. Chem. Chem. Phys.*, 2012, **14**, 1235–1245.
71 X. F. Li, Q. K. Li, J. Cheng, L. Liu, Q. Yan, Y. Wu, X. H. Zhang, Z. Y. Wang, Q. Qiu and Y. Luo, *J. Am. Chem. Soc.*, 2016, **138**, 8706–8709.
72 Y. Wan, J. Xu and R. Lv, *Mater. Today*, 2019, **27**, 69–90.
73 C. Ling, X. Bai, Y. Ouyang, A. Du and J. Wang, *J. Phys. Chem. C*, 2018, **122**, 16842–16847.
74 G. Liu, L. Niu, Z. Ma, L. An, D. Qu, D. Wang, X. Wang and Z. Sun, *Nano Res.*, 2022, **15**, 5940–5945.
75 Z. Wei, J. He, Y. Yang, Z. Xia, Y. Feng and J. Ma, *J. Energy Chem.*, 2021, **53**, 303–308.
76 A. Jain, M. Bar Sadan and A. Ramasubramaniam, *J. Phys. Chem. C*, 2021, **125**, 19980–19990.
77 D. Yao, C. Tang, L. Li, B. Xia, A. Vasileff, H. Jin, Y. Zhang and S. Z. Qiao, *Adv. Energy Mater.*, 2020, **10**, 2001289.
78 Y. Yao, S. Zhu, H. Wang, H. Li and M. Shao, *Angew. Chem., Int. Ed.*, 2020, **59**, 10479–10483.
79 M. A. Legare, G. Belanger-Chabot, R. D. Dewhurst, E. Welz, I. Krummenacher, B. Engels and H. Braunschweig, *Science*, 2018, **359**, 896–900.
80 P. Chen, Y. Tong, C. Wu and Y. Xie, *Acc. Chem. Res.*, 2018, **51**, 2857–2866.
81 C. Tang, H. F. Wang and Q. Zhang, *Acc. Chem. Res.*, 2018, **51**, 881–889.
82 C. Yang, Y. Zhu, J. Liu, Y. Qin, H. Wang, H. Liu, Y. Chen, Z. Zhang and W. Hu, *Nano Energy*, 2020, **77**, 105126.
83 Z. He, Y. Jiang, X. Cui, Z. Liu, X. Meng, J. Wan and F. Ma, *ACS Appl. Nano Mater.*, 2022, **5**, 5470–5478.
84 J. Wang, G. Li, T. Wei, S. Zhou, X. Ji and X. Liu, *Nanoscale*, 2021, **13**, 3036–3041.
85 Y. Ling, F. M. D. Kazim, S. Ma, Q. Zhang, K. Qu, Y. Wang, S. Xiao, W. Cai and Z. Yang, *J. Mater. Chem. A*, 2020, **8**, 12996–13003.
86 Y. J. Mao, L. Wei, X. S. Zhao, Y. S. Wei, J. W. Li, T. Sheng, F. C. Zhu, N. Tian, Z. Y. Zhou and S. G. Sun, *Chem. Commun.*, 2019, **55**, 9335–9338.
87 S. Dou, X. Wang and S. Wang, *Small Methods*, 2019, **3**, 1800211.
88 H. Fei, T. Guo, Y. Xin, L. Wang, R. Liu, D. Wang, F. Liu and Z. Wu, *Appl. Catal., B*, 2022, **300**, 120733.
89 D. Guo, S. Wang, J. Xu, W. Zheng and D. Wang, *J. Energy Chem.*, 2022, **65**, 448–468.
90 K. Chu, Y.-p. Liu, Y.-b. Li, H. Zhang and Y. Tian, *J. Mater. Chem. A*, 2019, **7**, 4389–4394.
91 D. Bao, Q. Zhang, F. L. Meng, H. X. Zhong, M. M. Shi, Y. Zhang, J. M. Yan, Q. Jiang and X. B. Zhang, *Adv. Mater.*, 2017, **29**, 1604799.
92 B. Cui, J. Zhang, S. Liu, X. Liu, W. Xiang, L. Liu, H. Xin, M. J. Lefler and S. Licht, *Green Chem.*, 2017, **19**, 298–304.
93 M. Zhao, C. Guo, L. Gao, H. Yang, C. Liu, X. Kuang, X. Sun and Q. Wei, *ChemCatChem*, 2021, **13**, 4990–4997.
94 S. Chen, S. Perathoner, C. Ampelli, C. Mebrahtu, D. Su and G. Centi, *Angew. Chem., Int. Ed.*, 2017, **56**, 2699–2703.
95 J. Li, X. Zhu, T. Wang, Y. Luo and X. Sun, *Inorg. Chem. Front.*, 2019, **6**, 2682–2685.
96 B. Xu, L. Xia, F. Zhou, R. Zhao, H. Chen, T. Wang, Q. Zhou, Q. Liu, G. Cui, X. Xiong, F. Gong and X. Sun, *ACS Sustainable Chem. Eng.*, 2019, **7**, 2889–2893.
97 F. Lai, J. Feng, X. Ye, W. Zong, G. He, C. Yang, W. Wang, Y.-E. Miao, B. Pan, W. Yan, T. Liu and I. P. Parkin, *J. Mater. Chem. A*, 2020, **8**, 1652–1659.
98 C. Wang, L.-L. Gu, S.-Y. Qiu, J. Gao, Y.-C. Zhang, K.-X. Wang, J.-J. Zou, P.-J. Zuo and X.-D. Zhu, *Appl. Catal., B*, 2021, **297**, 120452.
99 Z. Geng, X. Kong, W. Chen, H. Su, Y. Liu, F. Cai, G. Wang and J. Zeng, *Angew. Chem., Int. Ed.*, 2018, **57**, 6054–6059.
100 L. Hu, A. Khaniya, J. Wang, G. Chen, W. E. Kaden and X. Feng, *ACS Catal.*, 2018, **8**, 9312–9319.

101 J. Wang, S. Chen, Z. Li, G. Li and X. Liu, *ChemElectroChem*, 2020, **7**, 1067–1079.
102 K. Kim, C.-Y. Yoo, J.-N. Kim, H. C. Yoon and J.-I. Han, *J. Electrochem. Soc.*, 2016, **163**, F1523–F1526.
103 B. Wang, T. Li, F. Gong, M. H. D. Othman and R. Xiao, *Fuel Process. Technol.*, 2022, **235**, 107380.
104 F. Zhou, L. M. Azofra, M. Ali, M. Kar, A. N. Simonov, C. McDonnell-Worth, C. Sun, X. Zhang and D. R. MacFarlane, *Energy Environ. Sci.*, 2017, **10**, 2516–2520.
105 S. Stevanovic and M. F. Costa Gomes, *J. Chem. Thermodyn.*, 2013, **59**, 65–71.
106 C. S. M. Kang, X. Zhang and D. R. MacFarlane, *J. Phys. Chem. C*, 2018, **122**, 24550–24558.
107 B. H. R. Suryanto, C. S. M. Kang, D. Wang, C. Xiao, F. Zhou, L. M. Azofra, L. Cavallo, X. Zhang and D. R. MacFarlane, *ACS Energy Lett.*, 2018, **3**, 1219–1224.
108 S. Sun, X. Zhang, J. Cui, Q. Yang and S. Liang, *Nanoscale*, 2019, **11**, 15739–15762.
109 W. Zhang, Y. Shen, F. Pang, D. Quek, W. Niu, W. Wang and P. Chen, *ACS Appl. Mater. Interfaces*, 2020, **12**, 41613–41619.
110 A. Xie, L. Xiao, Q. Qiao and J. Liu, *J. Wuhan Univ. Technol., Mater. Sci. Ed.*, 2022, **37**, 807–814.
111 N. Tian, Z. Y. Zhou, S. G. Sun, Y. Ding and Z. L. Wang, *Science*, 2007, **316**, 732–735.
112 C. Xiao, B.-A. Lu, P. Xue, N. Tian, Z.-Y. Zhou, X. Lin, W.-F. Lin and S.-G. Sun, *Joule*, 2020, **4**, 2562–2598.
113 S. Yu, Q. Wang, J. Wang, Y. Xiang, X. Niu and T. Li, *Int. J. Hydrogen Energy*, 2021, **46**, 14331–14337.
114 C. Zhang, S. Liu, T. Chen, Z. Li and J. Hao, *Chem. Commun.*, 2019, **55**, 7370–7373.
115 M. Wang, F. Li and J. Liu, *RSC Adv.*, 2020, **10**, 29575–29579.
116 Z. Wang, K. Zheng, S. Liu, Z. Dai, Y. Xu, X. Li, H. Wang and L. Wang, *ACS Sustainable Chem. Eng.*, 2019, **7**, 11754–11759.
117 K. Chu, H. Nan, Q. Li, Y. Guo, Y. Tian and W. Liu, *J. Energy Chem.*, 2021, **53**, 132–138.
118 J. Wang, H. Nan, Y. Tian and K. Chu, *ACS Sustainable Chem. Eng.*, 2020, **8**, 12733–12740.
119 L. Zhang, X. Ji, X. Ren, Y. Ma, X. Shi, Z. Tian, A. M. Asiri, L. Chen, B. Tang and X. Sun, *Adv. Mater.*, 2018, **30**, e1800191.
120 X. Li, T. Li, Y. Ma, Q. Wei, W. Qiu, H. Guo, X. Shi, P. Zhang, A. M. Asiri, L. Chen, B. Tang and X. Sun, *Adv. Energy Mater.*, 2018, **8**, 1801357.
121 J. Liu, M. S. Kelley, W. Wu, A. Banerjee, A. P. Douvalis, J. Wu, Y. Zhang, G. C. Schatz and M. G. Kanatzidis, *Proc. Natl. Acad. Sci. U. S. A.*, 2016, **113**, 5530–5535.
122 X.-f. Zheng, J.-l. Xia, Z.-y. Nie, Y. Wang, Y. Yu, N. Ei Houda Bouroubi, J.-h. Chen and H.-c. Liu, *Chem. Eng. J.*, 2022, **442**, 136350.
123 X. Zhao, X. Lan, D. Yu, H. Fu, Z. Liu and T. Mu, *Chem. Commun.*, 2018, **54**, 13010–13013.
124 W. Xiong, Z. Guo, S. Zhao, Q. Wang, Q. Xu and X. Wang, *J. Mater. Chem. A*, 2019, **7**, 19977–19983.
125 D. Feng, X. Zhang, Y. Sun and T. Ma, *Nano Mater. Sci.*, 2020, **2**, 132–139.
126 H. Du, C. Yang, W. Pu, L. Zeng and J. Gong, *ACS Sustainable Chem. Eng.*, 2020, **8**, 10572–10580.
127 T. Chen, H. Ying, C. Zhang, J. Bi, Z. Li and J. Hao, *Chem. Commun.*, 2021, **57**, 6688–6691.
128 L. Gao, C. Guo, M. Zhao, H. Yang, X. Ma, C. Liu, X. Liu, X. Sun and Q. Wei, *ACS Appl. Mater. Interfaces*, 2021, **13**, 50027–50036.
129 Y. Guo, Y. Cheng, Q. Li and K. Chu, *J. Energy Chem.*, 2021, **56**, 259–263.
130 Z. Ma, C. Xiao, Z. Cui, W. Du, Q. Li, R. Sa and C. Sun, *J. Mater. Chem. A*, 2021, **9**, 6945–6954.
131 S. Yang, W. Ye, D. Zhang, X. Fang and D. Yan, *Inorg. Chem. Front.*, 2021, **8**, 1762–1770.
132 Y. Sun, S. Ding, B. Xia, J. Duan, M. Antonietti and S. Chen, *Angew. Chem., Int. Ed.*, 2022, **61**, e202115198.
133 B. M. Hoffman, D. Lukoyanov, Z. Y. Yang, D. R. Dean and L. C. Seefeldt, *Chem. Rev.*, 2014, **114**, 4041–4062.
134 S. L. Foster, S. I. P. Bakovic, R. D. Duda, S. Maheshwari, R. D. Milton, S. D. Minteer, M. J. Janik, J. N. Renner and L. F. Greenlee, *Nat. Catal.*, 2018, **1**, 490–500.
135 S. Chen, X. Liu, J. Xiong, L. Mi and Y. Li, *Mater. Today Nano*, 2022, **18**, 100202.
136 N. R. Singstock and C. B. Musgrave, *J. Am. Chem. Soc.*, 2022, **144**, 12800–12806.
137 K. Lu, F. Xia, B. Li, Y. Liu, I. B. Abdul Razak, S. Gao, J. Kaelin, D. E. Brown and Y. Cheng, *ACS Nano*, 2021, **15**, 16887–16895.
138 L. Zeng, S. Chen, J. van der Zalm, X. Li and A. Chen, *Chem. Commun.*, 2019, **55**, 7386–7389.
139 J. Zhang, X. Tian, M. Liu, H. Guo, J. Zhou, Q. Fang, Z. Liu, Q. Wu and J. Lou, *J. Am. Chem. Soc.*, 2019, **141**, 19269–19275.
140 L. Niu, D. Wang, K. Xu, W. Hao, L. An, Z. Kang and Z. Sun, *Nano Res.*, 2021, **14**, 4093–4099.
141 J. Guo, T. Tadesse Tsega, I. Ul Islam, A. Iqbal, J. Zai and X. Qian, *Chin. Chem. Lett.*, 2020, **31**, 2487–2490.
142 H. Y. Su, L. L. Chen, Y. Z. Chen, R. Si, Y. T. Wu, X. N. Wu, Z. G. Geng, W. H. Zhang and J. Zeng, *Angew. Chem., Int. Ed.*, 2020, **59**, 20411–20416.
143 Z. Y. Niu, L. Jiao, T. Zhang, X. M. Zhao, X. F. Wang, Z. Tan, L. Z. Liu, S. Chen and X. Z. Song, *ACS Appl. Mater. Interfaces*, 2022, **14**, 55559–55567.
144 H. Wang, W. Fu, X. Yang, Z. Huang, J. Li, H. Zhang and Y. Wang, *J. Mater. Chem. A*, 2020, **8**, 6926–6956.
145 M. Kim, M. A. R. Anjum, M. Choi, H. Y. Jeong, S. H. Choi, N. Park and J. S. Lee, *Adv. Funct. Mater.*, 2020, **30**, 2002536.
146 J. Liu, W. Kong, Z. Jin, Y. Han, J. Sun, L. Ma, Y. Niu and Y. Xu, *J. Mater. Chem. A*, 2020, **8**, 19278–19282.
147 X.-Z. Song, F.-F. Sun, Y.-L. Meng, Z.-W. Wang, Q.-F. Su and Z. Tan, *New J. Chem.*, 2019, **43**, 3601–3608.
148 H. Ding, H. Liu, W. Chu, C. Wu and Y. Xie, *Chem. Rev.*, 2021, **121**, 13174–13212.
149 Y. Xu, X. Jiang, G. Shao, H. Xiang, S. Si, X. Li, T. S. Hu, G. Hong, S. Dong, H. Li, Y. Feng and S. Liu, *Energy Environ. Mater.*, 2020, **4**, 117–125.
150 C. Ma, D. Liu, Y. Zhang, J. Yong Lee, J. Tian, B. Liu and S. Yan, *Chem. Eng. J.*, 2022, **430**, 132694.

151 X. Z. Song, W. Y. Zhu, J. C. Ni, Y. H. Zhao, T. Zhang, Z. Tan, L. Z. Liu and X. F. Wang, *ACS Appl. Mater. Interfaces*, 2022, **14**(29), 33151–33160.
152 X. Zhao, X. Zhang, Z. Xue, W. Chen, Z. Zhou and T. Mu, *J. Mater. Chem. A*, 2019, **7**, 27417–27422.
153 E. Hu, Y. Yao, Y. Cui and G. Qian, *Mater. Today Nano*, 2021, **15**, 100124.
154 C. Li, X. Sun, Y. Yao and G. Hong, *Mater. Today Nano*, 2021, **13**, 100105.
155 W. Ma, F. Wu, P. Yu and L. Mao, *Chem. Sci.*, 2021, **12**, 7908–7917.
156 Z. Li, M. Song, W. Zhu, W. Zhuang, X. Du and L. Tian, *Coord. Chem. Rev.*, 2021, **439**, 213946.
157 X. Z. Song, N. Zhang, X. F. Wang and Z. Tan, *Mater. Today Energy*, 2021, **19**, 100597.
158 Y. Yang, S. Feng, J. Su, Y. Gong and J. Wang, *ACS Sustainable Chem. Eng.*, 2022, **10**, 14064–14072.
159 Y. Li, Z. Yin, M. Cui, S. Chen and T. Ma, *Mater. Today Energy*, 2020, **18**, 100565.
160 S. Chen, M. Cui, Z. Yin, J. Xiong, L. Mi and Y. Li, *ChemSusChem*, 2021, **14**, 73–93.
161 X.-Z. Song, Y.-H. Zhao, W.-B. Yang, Y.-L. Meng, X. Chen, Z.-Y. Niu, X.-F. Wang and Z. Tan, *ACS Appl. Nano Mater.*, 2021, **4**, 13450–13458.
162 X. Z. Song, H. Wang, Z. Li, Y. L. Meng, Z. Tan and M. Zhu, *Chem. Commun.*, 2021, **57**, 3022–3025.
163 X. Song, S. Song, D. Wang and H. Zhang, *Small Methods*, 2021, **5**, e2001000.
164 H. He, H.-M. Wen, H.-K. Li and H.-W. Zhang, *Coord. Chem. Rev.*, 2022, **471**, 214761.
165 K. A. Adegoke, O. R. Adegoke, R. A. Adigun, N. W. Maxakato and O. S. Bello, *Coord. Chem. Rev.*, 2022, **473**, 214817.
166 L. Xiao, Z. Wang and J. Guan, *Coord. Chem. Rev.*, 2022, **472**, 214777.
167 L. Zou, Y. S. Wei, C. C. Hou, C. Li and Q. Xu, *Small*, 2021, **17**, e2004809.
168 Y. Pan, R. Abazari, Y. Wu, J. Gao and Q. Zhang, *Electrochem. Commun.*, 2021, **126**, 107024.
169 Z. H. Wang, X. F. Wang, Z. Tan and X. Z. Song, *Mater. Today Energy*, 2021, **19**, 100618.
170 S. Chen, H. Jang, J. Wang, Q. Qin, X. Liu and J. Cho, *J. Mater. Chem. A*, 2020, **8**, 2099–2104.
171 L. Zeng, X. Li, S. Chen, J. Wen, W. Huang and A. Chen, *J. Mater. Chem. A*, 2020, **8**, 7339–7349.
172 B. Li, X. Yu, H. Pang, Q. Shen, Y. Hou, H. Ma and J. Xin, *Chem. Commun.*, 2020, **56**, 7199–7202.
173 G. Wang, T. Chen, C. J. Gomez-Garcia, F. Zhang, M. Zhang, H. Ma, H. Pang, X. Wang and L. Tan, *Small*, 2020, **16**, e2001626.
174 J. Wu, Z. Wang, S. Li, S. Niu, Y. Zhang, J. Hu, J. Zhao and P. Xu, *Chem. Commun.*, 2020, **56**, 6834–6837.
175 K. Chu, Q. Q. Li, Y. H. Cheng and Y. P. Liu, *ACS Appl. Mater. Interfaces*, 2020, **12**, 11789–11796.
176 H. Xian, H. Guo, Z. Chen, G. Yu, A. A. Alshehri, K. A. Alzahrani, F. Hao, R. Song and T. Li, *ACS Appl. Mater. Interfaces*, 2020, **12**, 2445–2451.
177 Q. Qin, T. Heil, M. Antonietti and M. Oschatz, *Small Methods*, 2018, **2**, 1800202.
178 J. Yao, Y. Zhou, J. M. Yan and Q. Jiang, *Adv. Energy Mater.*, 2021, **11**, 2003701.
179 W. Yu, M. D. Porosoff and J. G. Chen, *Chem. Rev.*, 2012, **112**, 5780–5817.
180 J. D. Lee, J. B. Miller, A. V. Shneidman, L. Sun, J. F. Weaver, J. Aizenberg, J. Biener, J. A. Boscoboinik, A. C. Foucher, A. I. Frenkel, J. E. S. van der Hoeven, B. Kozinsky, N. Marcella, M. M. Montemore, H. T. Ngan, C. R. O'Connor, C. J. Owen, D. J. Stacchiola, E. A. Stach, R. J. Madix, P. Sautet and C. M. Friend, *Chem. Rev.*, 2022, **122**, 8758–8808.
181 A. Das, A. S. Nair, S. C. Mandal and B. Pathak, *ACS Appl. Nano Mater.*, 2021, **4**, 7758–7770.
182 R. Chen, D. Chen and Y. Xiao, *Mater. Today Energy*, 2021, **20**, 100684.
183 A. Das, S. C. Mandal, A. S. Nair and B. Pathak, *ACS Phys. Chem. Au*, 2022, **2**, 125–135.
184 J. Zhang, Y. Ji, P. Wang, Q. Shao, Y. Li and X. Huang, *Adv. Funct. Mater.*, 2019, **30**, 1906579.
185 X. Chen, H. Yin, X. Yang, W. Zhang, D. Xiao, Z. Lu, Y. Zhang and P. Zhang, *Inorg. Chem.*, 2022, **61**, 20123–20132.
186 C. Huang, L. Shang, P. Han, Z. Gu, A. M. Al-Enizi, T. M. Almutairi, N. Cao and G. Zheng, *J. Colloid Interface Sci.*, 2019, **552**, 312–318.
187 A. Biswas, S. Bhardwaj, T. Boruah and R. S. Dey, *Mater. Adv.*, 2022, **3**, 5207–5233.
188 S. Carenco, D. Portehault, C. Boissiere, N. Mezailles and C. Sanchez, *Chem. Rev.*, 2013, **113**, 7981–8065.
189 X. Yang, C. Shang, S. Zhou and J. Zhao, *Nanoscale Horiz.*, 2020, **5**, 1106–1115.
190 S. Zhou, X. Yang, W. Pei, Z. Jiang and J. Zhao, *JPhys Energy*, 2020, **3**, 012002.
191 F. Ma, Y. Jiao, G. Gao, Y. Gu, A. Bilic, Z. Chen and A. Du, *Nano Lett.*, 2016, **16**, 3022–3028.
192 C. Liu, Q. Li, C. Wu, J. Zhang, Y. Jin, D. R. MacFarlane and C. Sun, *J. Am. Chem. Soc.*, 2019, **141**, 2884–2888.
193 X. Liu, Y. Jiao, Y. Zheng and S.-Z. Qiao, *ACS Catal.*, 2020, **10**, 1847–1854.
194 Z. Chen, J. Zhao, L. Yin and Z. Chen, *J. Mater. Chem. A*, 2019, **7**, 13284–13292.
195 X. Mao, S. Zhou, C. Yan, Z. Zhu and A. Du, *Phys. Chem. Chem. Phys.*, 2019, **21**, 1110–1116.
196 W. Song, Z. Fu, L. Fu and C. He, *J. Electrochem. Soc.*, 2021, **168**, 066503.
197 G. Qin, Q. Cui, A. Du, W. Wang and Q. Sun, *ChemCatChem*, 2019, **11**, 2624–2633.
198 Z. Pu, T. Liu, G. Zhang, X. Liu, M. A. Gauthier, Z. Chen and S. Sun, *Small Methods*, 2021, **5**, e2100699.
199 L. Ge, W. Xu, C. Chen, C. Tang, L. Xu and Z. Chen, *J. Phys. Chem. Lett.*, 2020, **11**, 5241–5247.
200 S. Qi, Y. Fan, L. Zhao, W. Li and M. Zhao, *Appl. Surf. Sci.*, 2021, **536**, 147742.
201 W. Chen, J. Pei, C. T. He, J. Wan, H. Ren, Y. Wang, J. Dong, K. Wu, W. C. Cheong, J. Mao, X. Zheng, W. Yan, Z. Zhuang,

C. Chen, Q. Peng, D. Wang and Y. Li, *Adv. Mater.*, 2018, **30**, e1800396.
202 Y. Yao, S. Hu, W. Chen, Z.-Q. Huang, W. Wei, T. Yao, R. Liu, K. Zang, X. Wang, G. Wu, W. Yuan, T. Yuan, B. Zhu, W. Liu, Z. Li, D. He, Z. Xue, Y. Wang, X. Zheng, J. Dong, C.-R. Chang, Y. Chen, X. Hong, J. Luo, S. Wei, W.-X. Li, P. Strasser, Y. Wu and Y. Li, *Nat. Catal.*, 2019, **2**, 304–313.
203 Z. Fu, M. Wu, Q. Li, C. Ling and J. Wang, *Mater. Horiz.*, 2023, **10**, 852–858.
204 L. Li, W. Yu, W. Gong, H. Wang, C.-L. Chiang, Y. Lin, J. Zhao, L. Zhang, J.-M. Lee and G. Zou, *Appl. Catal., B*, 2023, **321**, 122038.
205 L. Liu and A. Corma, *Chem. Rev.*, 2018, **118**, 4981–5079.
206 Y. Wang, J. Mao, X. Meng, L. Yu, D. Deng and X. Bao, *Chem. Rev.*, 2019, **119**, 1806–1854.
207 Y. Peng, B. Lu and S. Chen, *Adv. Mater.*, 2018, **30**, e1801995.
208 X. Li, P. Cui, W. Zhong, J. Li, X. Wang, Z. Wang and J. Jiang, *Chem. Commun.*, 2016, **52**, 13233–13236.
209 H. Jeong, S. Shin and H. Lee, *ACS Nano*, 2020, **14**, 14355–14374.
210 H. Yang, Y. Liu, Y. Luo, S. Lu, B. Su and J. Ma, *ACS Sustainable Chem. Eng.*, 2020, **8**, 12809–12816.
211 H. Zhang, G. Liu, L. Shi and J. Ye, *Adv. Energy Mater.*, 2018, **8**, 1701343.
212 R. Qin, P. Liu, G. Fu and N. Zheng, *Small Methods*, 2018, **2**, 1700286.
213 Y. Liu, Z. Zhao, W. Wei, X. Jin, G. Wang, K. Li and Y. Lin, *ACS Appl. Nano Mater.*, 2021, **4**, 13001–13009.
214 Q. Zhang and J. Guan, *Adv. Funct. Mater.*, 2020, **30**, 2000768.
215 X. Guo and S. Huang, *Electrochim. Acta*, 2018, **284**, 392–399.
216 C. He, Z.-Y. Wu, L. Zhao, M. Ming, Y. Zhang, Y. Yi and J.-S. Hu, *ACS Catal.*, 2019, **9**, 7311–7317.
217 W. Wei, X. Shi, P. Gao, S. Wang, W. Hu, X. Zhao, Y. Ni, X. Xu, Y. Xu, W. Yan, H. Ji and M. Cao, *Nano Energy*, 2018, **52**, 29–37.
218 M. Wang, S. Liu, T. Qian, J. Liu, J. Zhou, H. Ji, J. Xiong, J. Zhong and C. Yan, *Nat. Commun.*, 2019, **10**, 341.
219 D. Liu, H. Ai, W. T. Lou, F. Li, K. H. Lo, S. Wang and H. Pan, *Sustainable Energy Fuels*, 2020, **4**, 3773–3779.
220 B. Wang, S. Huang, L. Yang, Q. Fu and Y. Bu, *J. Phys. Chem. C*, 2021, **125**, 14253–14262.
221 W. Shan and G. Wang, *J. Phys. Chem. C*, 2021, **125**, 16004–16012.
222 Y. Wang, H. Li, F. Peng and F. Gao, *Chem. Eng. J.*, 2022, **445**, 136692.
223 H. Zhang, C. Cui and Z. Luo, *J. Phys. Chem. C*, 2020, **124**, 6260–6266.
224 J. Li, S. Chen, F. Quan, G. Zhan, F. Jia, Z. Ai and L. Zhang, *Chem*, 2020, **6**, 885–901.
225 X. Lv, W. Wei, B. Huang, Y. Dai and T. Frauenheim, *Nano Lett.*, 2021, **21**, 1871–1878.
226 H. Li, Z. Zhao, Q. Cai, L. Yin and J. Zhao, *J. Mater. Chem. A*, 2020, **8**, 4533–4543.
227 F. Li and Q. Tang, *Nanoscale*, 2019, **11**, 18769–18778.
228 W. Ren, X. Tan, J. Qu, S. Li, J. Li, X. Liu, S. P. Ringer, J. M. Cairney, K. Wang, S. C. Smith and C. Zhao, *Nat. Commun.*, 2021, **12**, 1449.
229 D. Ma, Z. Zeng, L. Liu and Y. Jia, *J. Energy Chem.*, 2021, **54**, 501–509.
230 D. Ma, Z. Zeng, L. Liu, X. Huang and Y. Jia, *J. Phys. Chem. C*, 2019, **123**, 19066–19076.
231 W. Cui, B. Geng, X. Chu, J. He, L. Jia, X. Han, X. Wang, S. Song and H. Zhang, *Nano Res.*, 2022, DOI: **10.1007/s12274-022-5246-x**.
232 S. Gao, X. Liu, Z. Wang, Y. Lu, R. Sa, Q. Li, C. Sun, X. Chen and Z. Ma, *J. Colloid Interface Sci.*, 2023, **630**, 215–223.
233 S. Zhang, M. Han, T. Shi, H. Zhang, Y. Lin, X. Zheng, L. R. Zheng, H. Zhou, C. Chen, Y. Zhang, G. Wang, H. Yin and H. Zhao, *Nat. Sustain.*, 2022, **6**, 169–179.
234 T. Zhang, A. G. Walsh, J. Yu and P. Zhang, *Chem. Soc. Rev.*, 2021, **50**, 569–588.
235 R. T. Hannagan, G. Giannakakis, M. Flytzani-Stephanopoulos and E. C. H. Sykes, *Chem. Rev.*, 2020, **120**, 12044–12088.
236 Z. Xu, Z. Ao, M. Yang and S. Wang, *J. Hazard. Mater.*, 2022, **424**, 127427.
237 K. Chu, Y.-h. Cheng, Q.-q. Li, Y.-p. Liu and Y. Tian, *J. Mater. Chem. A*, 2020, **8**, 5865–5873.
238 Z. Chen, H. Niu, J. Ding, H. Liu, P. H. Chen, Y. H. Lu, Y. R. Lu, W. Zuo, L. Han, Y. Guo, S. F. Hung and Y. Zhai, *Angew. Chem., Int. Ed.*, 2021, **133**, 25608–25614.
239 J. Chen, H. Cheng, L.-X. Ding and H. Wang, *Mater. Chem. Front.*, 2021, **5**, 5954–5969.
240 Y. Yang, M. Luo, W. Zhang, Y. Sun, X. Chen and S. Guo, *Chem*, 2018, **4**, 2054–2083.
241 I. E. Khalil, C. Xue, W. Liu, X. Li, Y. Shen, S. Li, W. Zhang and F. Huo, *Adv. Funct. Mater.*, 2021, **31**, 2010052.
242 Z. Xu, Z. Liang, W. Guo and R. Zou, *Coord. Chem. Rev.*, 2021, **436**, 213824.
243 Z. Chen, C. Liu, L. Sun and T. Wang, *ACS Catal.*, 2022, **12**, 8936–8975.